Author(s): Leguillon, R.; Petrache, C.M.; Zerrouki, T.; Konstantinopoulos, T.; Hauschild, Karl; Korichi, A.; Lopez-Martens, Araceli; Frauendorf, S.; Ragnarsson, I.; Greenlees, Paul; Jakobsson, Ulrika; Jones, Peter; Julin, Rauno; Juutinen, Sakari; Ketelhut, Steffen; Leino, Matti; Nieminen, Päivi; Nyman, Markus; Peura, Pauli; Rahkila, Panu; Ruotsalainen, Panu; Sandzelius, Mikael; Sarén, Jan; Scholey, Catherine; Sorri, Juha; Uusitalo, Juha;

Title: High-spin spectroscopy of 140Nd

Year: 2013

Version:

Please cite the original version:

Leguillon, R., Petrache, C.M., Zerrouki, T., Konstantinopoulos, T., Hauschild, K., Korichi, A., Lopez-Martens, A., Frauendorf, S., Ragnarsson, I., Greenlees, P., Jakobsson, U., Jones, P., Julin, R., Juutinen, S., Ketelhut, S., Leino, M., Nieminen, P., Nyman, M., Peura, P., . . . Cullen, D. (2013). High-spin spectroscopy of 140Nd. Physical Review C, 88(1), Article 014323. https://doi.org/10.1103/PhysRevC.88.014323

PHYSICAL REVIEW C **88**, 014323 (2013)

High-spin spectroscopy of ^{140}Nd

R. Leguillon, C. M. Petrache, T. Zerrouki, T. Konstantinopoulos, K. Hauschild, A. Korichi, and A. Lopez-Martens
Centre de Sciences Nucléaires et de Sciences de la Matière, Université Paris-Sud and CNRS/IN2P3, Bât. 104-108, F-91405 Orsay, France

S. Frauendorf
Department of Physics, University of Notre Dame, Notre Dame, Indiana 46556, USA

I. Ragnarsson
Division of Mathematical Physics, LTH, Lund University, P.O. Box 118, SE-221 00 Lund, Sweden

P. T. Greenlees, U. Jakobsson, P. Jones,* R. Julin, S. Juutinen, S. Ketelhut, M. Leino, P. Nieminen, M. Nyman, P. Peura, P. Rahkila, P. Ruotsalainen, M. Sandzelius, J. Saren, C. Scholey, J. Sorri, and J. Uusitalo
Department of Physics, University of Jyväskylä, Jyväskylä, FIN-40014, Finland

H. Hübel, A. Neußer-Neffgen, A. Al-Khatib, A. Bürger, N. Nenoff, and A. K. Singh†
Helmholtz-Institut für Strahlen- und Kernphysik, Universität Bonn, Nuallee 14-16, D-53115 Bonn, Germany

D. Curien
Departement de Recherches Subatomiques, Institut Pluridisciplinaire Hubert Curien, DRS-IPHC, 23 rue du Loess, B.P. 28, F-67037 Strasbourg, France

G. B. Hagemann, B. Herskind, and G. Sletten
Niels Bohr Institute, Blegdamsvej 17, DK-2100 Copenhagen, Denmark

P. Fallon
Nuclear Science Division, Lawrence Berkeley National Laboratory, Berkeley, California 94720, USA

A. Görgen
Departement de Physics, University of Oslo, Oslo, Norway

P. Bednarczyk
The Niewodniczanski Institute of Nuclear Physics, Polish Academy of Sciences, ul. Radzikowskiego 152, PL-31342 Krakow, Poland

D. M. Cullen
School of Physics and Astronomy, Schuster Laboratory, The University of Manchester, Manchester M13 9PL, United Kingdom
(Received 4 June 2013; published 24 July 2013)

The population of the high-spin states in ^{140}Nd was investigated using the reaction ^{96}Zr(^{48}Ca,4n). The results from two experiments, one with the EUROBALL array and one with the JUROGAM II + RITU + GREAT setup employing the recoil decay tagging technique, have been combined to develop a very detailed level scheme for ^{140}Nd. Twelve bands of quadrupole transitions and eleven bands of dipole transitions were identified and their connections to low-lying states were established. Calculations using the cranked Nilsson-Strutinsky and the tilted axis cranking models were used to interpret the observed structures. The overall good agreement between the experimental results and the calculations assuming a triaxial shape of the nucleus strongly support the existence of a stable triaxial shape at high spins in this mass region.

DOI: 10.1103/PhysRevC.88.014323 PACS number(s): 21.10.Re, 21.60.Ev, 23.20.Lv, 27.60.+j

I. INTRODUCTION

The nuclei with $A \sim 140$ having a few holes in the $N = 82$ shell closure are spherical or only slightly deformed in the ground state [1]. They can be easily polarized by unpaired nucleons resulting from broken pairs. Depending on the orbitals close to the Fermi surfaces for protons and neutrons, the nucleus can evolve from one shape to another with

*Present address: iThemba LABS, P.O. Box 722, Somerset West 7129, South Africa.

†Present address: Department of Physics and Metrology, Indian Institue of Technology Kharagpur, Kharagpur, IN-721303, India.

increasing excitation energy, or can exhibit different coexisting shapes in certain spin ranges: spherical and triaxial at medium spins, and triaxial and highly deformed or superdeformed at high spins. At low spins the presence of isomers based on simple particle-hole excitations helps to establish the active quasiparticle configurations and test the suitability of various nuclear potentials, whereas at high spins the combined contribution of neutron holes in the $N = 82$ core and neutron particles in the high-j orbitals above the $N = 82$ gap drive the nuclear shape toward a stable triaxial shape with $\gamma \approx +30^\circ$ [2,3]. At very high spins superdeformation is observed [4]. The analysis of the data coming from large γ arrays is made difficult by the presence of low-energy γ rays and isomeric states that often are not measured in the performed experiments. Such a situation is encountered in the weakly deformed Nd nuclei with neutron numbers close to the $N = 82$ shell closure, with irregular sequences of transitions and possible yrast traps. In fact, isomeric states were observed in ^{138}Nd ($I^\pi = 10^+$, $T_{1/2} = 410$ ns) [5], in ^{139}Nd ($I^\pi = 23/2^+$, $T_{1/2} = 272$ ns) [6], and in ^{140}Nd ($I^\pi = 10^+$, $T_{1/2} = 32$ ns and $I^\pi = 7^-$, $T_{1/2} = 600$ μs) [7].

New experimental data were recently published for the ^{140}Nd nucleus, which has a $I^\pi = 20^+$ isomeric state at $E_x = 7.43$ MeV [8], with $T_{1/2} = 1.23$ μs [9]. This lifetime supports the $I^\pi = 20^+$ spin-parity assignment and the interpretation as a six-quasiparticle spherical configuration that coexists with the surrounding triaxial bands.

The ^{140}Nd nucleus was also studied in a high-statistics experiment using the EUROBALL array and the results of the experiment have been published in two recent papers [3,4]. Many bands were observed at high spins and some of them were also linked to low-lying states. Theoretical calculations with the cranked Nilsson-Strutinsky (CNS) model were used to interpret the observed bands, and the existence of stable triaxiality at high spin in this mass region was claimed.

However, even if the level scheme was developed up to very high spins, no transitions feeding the 20^+ isomeric state from higher-lying states were observed. We have therefore performed a dedicated experiment to search for the transitions populating the 20^+ isomer. As the lifetime of the isomer of 1.23 μs is long enough to employ the recoil-tagging technique, we used the high efficiency gas-filled recoil mass separator RITU and the two high efficiency setups for γ-ray detection, JUROGAM II and GREAT, placed at the entrance and at the focal plane of the spectrometer, respectively. The results on the population of the 20^+ isomer in ^{140}Nd are published in Ref. [10]. This recoil isomer tagging experiment revealed states which were unobserved in the prompt coincidence experiment with EUROBALL, and induced us to reanalyze the data of the EUROBALL experiment in order to clarify and understand the newly observed transitions. The combined analysis of the two experiments led to the observation of many new bands and weak transitions which enabled the construction of a much more clear and complete high-spin level scheme for ^{140}Nd. The present level scheme includes 12 bands of only quadrupole transitions, 11 dipole bands, and many interconnecting transitions, which lead to the determination of the excitation energy and spins for most of the observed states. In many cases also the parity was determined.

The configuration assignment to the observed bands is made with the CNS and the tilted axis cranking (TAC) models. For the dipole bands, the new procedure introduced recently in the interpretation of the low- and medium-spin bands in the neighboring ^{138}Nd nucleus is used [11].

The details of the experimental setups are presented in Sec. II. The results of the data analysis are presented in Sec. III. The configurations of the different bands are discussed in Sec. IV. Finally, the summary is given in Sec. V.

II. EXPERIMENTAL DETAILS

A. JUROGAM II + RITU + GREAT experiment

In the JUROGAM II experiment, high-spin states in ^{140}Nd have been populated via the ^{96}Zr(^{48}Ca,4n) reaction, with a 180 MeV ^{48}Ca beam provided by the K130 cyclotron at the University of Jyväskylä, Finland. The target consisted of a self-supporting ^{96}Zr foil of 735 μg/cm^2 thickness. The experimental setup was composed of JUROGAM II + RITU + GREAT. The JUROGAM II array [12] placed at the entrance of the RITU spectrometer [13] is composed of 39 Compton-suppressed Ge detectors: 24 clover detectors and 15 coaxial tapered detectors. The clovers are placed on two rings at 75.5° (12 clovers) and 104.5° (12 clovers) symmetric with respect to 90°, while the tapered detectors are placed on two rings at backward angles of 133.6° (10 detectors) and 157.6° (5 detectors). The GREAT spectrometer [14] around the focal plane of RITU was composed of several types of detectors. A multi-wire proportional counter (MWPC) was used to measure the position of the recoils and to give the time reference for the delayed γ-γ coincidences and for the measurement of the time of flight of the recoils between the MWPC and a silicon DSSD detector placed downstream of the MWPC. Behind the DSSD was placed a segmented planar Ge detector of 12 cm × 6 cm corresponding to 24 × 12 segments with a thickness of 1.5 cm, used for the measurement of x rays and low-energy γ rays. For the measurement of high-energy γ rays, a large volume clover having each crystal segmented into four was placed just above the focal plane reaction chamber and two clovers were placed on the right and left sides of the reaction chamber. The JUROGAM II array has been used for a standard coincidence measurement of γ rays, while the time correlated events in JUROGAM II and GREAT were used to measure delayed γ-γ coincidences.

The trigerless total data readout (TDR) [15] time stamped the events, which were then sorted using the GRAIN code [16]. Events were created in GRAIN using the signal from the MWPC as a "trigger," with the energies of any gamma rays detected within a time window of [−5 μs, +10 μs] with respect to the time reference given by the MWPC being collected into an event. Given the lifetime of the 20^+ isomer in ^{140}Nd of 1.23 μs and the flight time through RITU of around 650 ns, this time window allowed us to measure the major part of the isomer decay and the delayed γ-γ coincidences. The event rate in the MWPC was around 13 kHz, which was low enough to avoid the overlap between successive events separated in average by 80 μs. The analysis was performed with the GAMMAWARE [17] and RADWARE [18,19] programs.

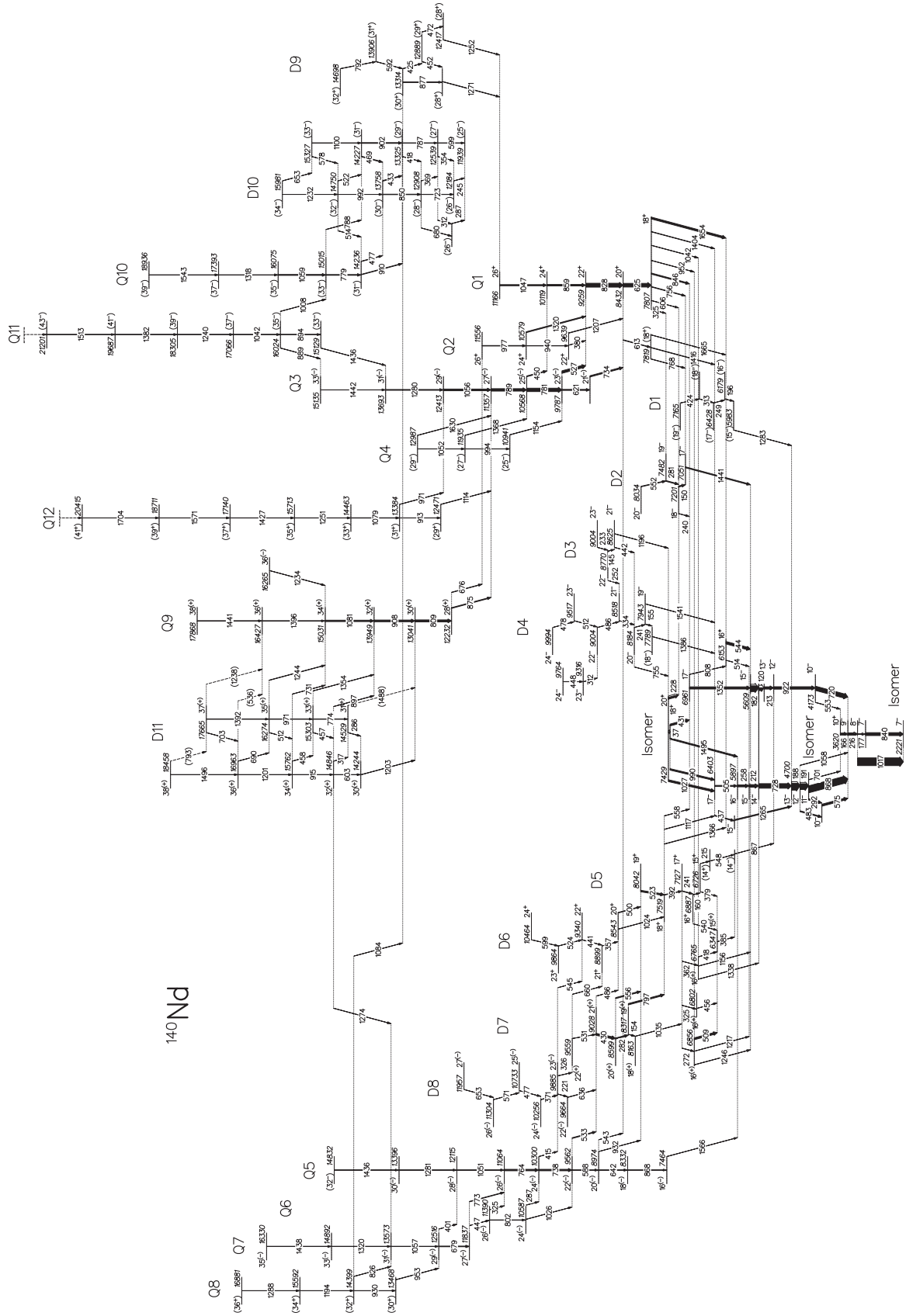

FIG. 1. Level scheme of ^{140}Nd in which all bands linked to low-lying states are drawn. The highest states of bands Q11 and Q12 have been cut to minimize the shrink of the figure.

A total of 5×10^9 events has been collected. Thanks to the high efficiency of the various γ-ray arrays, we produced γ-γ matrices for each array, i.e., one for JUROGAM II at the target position, and two for the Ge detectors at the focal plane: one for the clovers and one segmented planar Ge detector. The lifetime of the isomeric states in the nuclei implanted in the DSSD detector at the focal plane has been measured using γ-time matrices.

The transition multipolarities of the newly observed prompt transitions above the isomers have been extracted from the anisotropies using asymmetric γ-γ matrices constructed for the JUROGAM II array.

B. EUROBALL experiment

In the EUROBALL experiment, high-spin states in ^{140}Nd have been populated via the ^{96}Zr(^{48}Ca,4n) reaction induced by a 195 MeV ^{48}Ca beam delivered by the Vivitron tandem accelerator at the Institut de Recherches Subatomiques, Strasbourg. A self-supporting ^{96}Zr foil of 735 μg/cm^2 thickness was used as a target. Gamma-ray coincidences were measured with the EUROBALL spectrometer [20], consisting of 30 single, tapered Ge detectors, and 15 cluster and 26 clover composite Ge detectors, each surrounded by a BGO Compton-suppression shield. Out of the total number of 239 Ge crystals, 230 could be used in our analysis. Multiplicity information was obtained from the inner ball of 210 BGO detectors. Events were written to tape with the requirement that at least 11 BGO detectors of the inner ball and four Ge crystals before Compton suppression were in prompt coincidence. Presorting of the data, which included Compton suppression and add-back for the composite detectors, resulted in a total of 1.5×10^9 events with a γ-ray coincidence fold $\geqslant 3$. The γ-ray coincidences were sorted into three- and four-dimensional coincidence arrays (cube and hypercube, respectively), and the analysis was carried out with the RADWARE software package [18,19]. To determine the multipolarity of transitions, several gated matrices (with gates set on all detectors on specific transitions with known quadrupole and dipole character of ^{140}Nd) were sorted with all detectors on one axis and detectors at 90° and at forward/backward (f,b) angles, respectively, on the other axis. Gates were set on the axis with all detectors, and the anisotropy defined by the intensity ratio $W(\mathrm{f,b})/W(90^\circ)$, was determined for the transitions in the resulting spectra. The multipolarity of the new transitions identified in ^{140}Nd were assigned based on the comparison of the deduced anisotropies with the average anisotropies extracted for known pure $E2$ and $E1$ transitions in nuclei populated in the reaction, which have the values of 0.61 ± 0.03 and 0.28 ± 0.05, respectively.

III. RESULTS AND LEVEL SCHEME

The relevant part of the level scheme of ^{140}Nd is shown in Fig. 1. We do not draw all states and transitions, but only those which are relevant for the development of the level scheme at high spins. The information about the observed bands and their decays out, given in Table I, was obtained from the EUROBALL experiment. The highest transitions of bands Q11 and Q12 and the states in the ground-state band up to $I^\pi = 7^-$ were not drawn in the present level scheme to avoid shrinking it any further. However, the related information is given in Table I. Four bands published previously in Ref. [3], bands 8–11, are not linked to the low-lying states and will not be discussed in the present paper.

The large majority of the previously observed states are confirmed, but the combined results of the two experiments induce some important changes with respect to the previously published level schemes [3,8]. The most important one is the positive-parity assignment to the 16^+ state at 6153 keV, which is opposite to that assigned in Ref. [3]. The positive-parity assignment was considered and discussed as possible alternative in our previous paper [8], but the available information at that time was not sufficient to disentangle between positive and negative parity. The observation of many new transitions in the JUROGAM II experiment and the careful analysis of the data of the EUROBALL experiment lead to the identification of several new transitions which connect the different observed bands both at low and high spins. The anisotropies of the newly observed transitions allowed an unambiguous positive-parity assignment to the 16^+ state at 6153 keV, which has as a consequence the change of the parity of several high-spin bands with respect to the previous publication [3].

The task to establish the parity of the states at high spins is not easy. In our case, the existence of the long-lived 20^+ isomer [8] allowed us to assign the parity to some states on the basis of the expected weak strength of the transitions from the isomer to the states in question. In addition, we also observed three transitions of 1008, 1084, and 1274 keV connecting high-spin states of the bands Q11 and Q10, Q8 and D9, and D11 and Q8, respectively, whose anisotropies constrained the relative spin-parity of the bands.

A. The bands of quadrupole transitions (Q1–Q11)

Spectra obtained by doubly gating on selected transitions of the different Q bands are shown in Figs. 2–4.

The most populated band at high spins is Q1. Its decay is very fragmented and proceeds towards states of both positive and negative parity. This is an indication of a drastic shape change from nearly spherical to a triaxial shape induced by the occupation of the $h_{9/2}$ neutron intruder orbital from above the $N = 82$ shell closure (see the discussion in Sec. IV). We confirm all previously observed transitions deexciting the two 18^+ states populated by the 624 and 612 keV transitions, with the exception of the 859 keV transition which appears in the spectrum gated by 612 keV only because it is a member of the Q1 band. We identified four new transitions of 325, 952, 1042, and 1665 keV deexciting the 18^+ states. In our previous paper [3] we have clearly identified the bands Q1 and Q3. In the published level scheme there were also several irregular structures around the bands Q1 and Q3, which were not grouped into bands since no clear decay pattern was identified. The transitions of those structures are now assigned to bands Q2, Q4, and D9. With the additional information from the JUROGAM II experiment, which indicates that band Q9 has a delayed decay [10], we could clearly identify the

TABLE I. Energies, intensities, anisotropies, multipolarities, and spin-parity assignments of γ-ray transitions of ^{140}Nd from the EUROBALL experiment. The transitions are grouped in bands and the transitions connecting a given band to low-lying states are listed at the end of each band separated by a blank line.

γ-ray energy[a]	E_i (keV)	Intensity[b]	Anisotropy[c]	Multipolarity	$J_i^\pi \rightarrow J_f^\pi$
Band Q1					
624.6	8432	20.5	0.65(3)	$E2$	$20^+ \rightarrow 18^+$
827.6	9259	21.9	0.67(9)	$E2$	$22^+ \rightarrow 20^+$
859.1	10119	8.2	0.80(10)	$E2$	$24^+ \rightarrow 22^+$
1046.7	11166	6.3	0.65(15)	$E2$	$26^+ \rightarrow 24^+$
324.6	7807		0.26(5)	$E1$	$18^+ \rightarrow 19^-$
605.6	7807	0.5	0.40(15)	$E1$	$18^+ \rightarrow 18^-$
612.7	8432	2.7			$18^+ \rightarrow (18^+)$
755.8	7807	2.7		$(E1)$	$18^+ \rightarrow 17^-$
768.4	7819				$(18^+) \rightarrow 17^-$
845.8	7807	6.0	0.26(5)	$E1$	$18^+ \rightarrow 17^-$
951.6	7807		0.83(13)	$E2$	$18^+ \rightarrow 16^+$
1041.9	7807		0.79(8)	$E2$	$18^+ \rightarrow 16^{(+)}$
1404.1	7807	1.9		$(E1)$	$18^+ \rightarrow 17^-$
1415.8	7819				$(18^+) \rightarrow 17^-$
1653.7	7807	9.6	0.84(22)	$E2$	$18^+ \rightarrow 16^+$
1665.0	7819				$(18^+) \rightarrow 16^+$
Band Q2					
940.4	10579		0.72(5)	$E2$	$24^+ \rightarrow 22^+$
976.5	11556	2.7	0.70(6)	$E2$	$26^+ \rightarrow 24^+$
379.9	9639		0.36(5)	$M1/E2$	$22^+ \rightarrow 22^+$
1207.1	9639		0.65(10)	$E2$	$22^+ \rightarrow 20^+$
1319.9	10579		0.65(7)	$E2$	$24^+ \rightarrow 22^+$
Band Q3					
620.7	9787	5.5	0.68(4)	$E2$	$23^{(-)} \rightarrow 21^{(-)}$
781.3	10568	19.2	0.68(3)	$E2$	$25^{(-)} \rightarrow 23^{(-)}$
788.7	11357	13.7	0.71(4)	$E2$	$27^{(-)} \rightarrow 25^{(-)}$
1055.8	12413	9.6	0.74(6)	$E2$	$29^{(-)} \rightarrow 27^{(-)}$
1280.4	13693	4.4	0.70(10)	$E2$	$31^{(-)} \rightarrow 29^{(-)}$
1441.6	15135	0.8			$(33^-) \rightarrow 31^{(-)}$
449.5	10568	4.4	0.31(5)	$E1$	$25^{(-)} \rightarrow 24^+$
527.3	9787	8.2	0.33(5)	$E1$	$23^{(-)} \rightarrow 22^+$
734.2	9166	6.0	0.33(5)	$E1$	$21^{(-)} \rightarrow 20^+$
Band Q4					
994.5	11935		0.74(10)	$E2$	$(27^-) \rightarrow (25^-)$
1051.9	12987				$(29^-) \rightarrow (27^-)$
1154.5	10941				$(25^-) \rightarrow 23^{(-)}$
1367.6	11935				$(27^-) \rightarrow 25^{(-)}$
1629.7	12987				$(29^-) \rightarrow 27^{(-)}$
Band Q5					
868.4	8332				$18^{(-)} \rightarrow (16^-)$
642.4	8974		0.72(10)	$E2$	$20^{(-)} \rightarrow 18^{(-)}$
587.6	9562	2.2	0.84(10)	$E2$	$22^{(-)} \rightarrow 20^{(-)}$
737.5	10300	6.8	0.76(5)	$E2$	$24^{(-)} \rightarrow 22^{(-)}$
764.4	11064	5.5	0.68(3)	$E2$	$26^{(-)} \rightarrow 24^{(-)}$
1051.0	12115	2.7	0.78(10)	$E2$	$28^{(-)} \rightarrow 26^{(-)}$
1281.1	13396	1.4	0.61(9)	$E2$	$30^{(-)} \rightarrow 28^{(-)}$
1436.3	14832	0.5			$(32^-) \rightarrow 30^{(-)}$
415.1	10300			$(E1)$	$24^{(-)} \rightarrow 23^{(+)}$
533.6	9562	4.1	0.25(3)	$E1$	$22^{(-)} \rightarrow 21^+$
542.7	8974		0.26(10)	$E1$	$20^{(-)} \rightarrow 20^+$
932.2	8974			$(E1)$	$20^{(-)} \rightarrow 19^+$
1566.4	7464				$(16^-) \rightarrow 16^-$

TABLE I. (*Continued*.)

γ-ray energy[a]	E_i (keV)	Intensity[b]	Anisotropy[c]	Multipolarity	$J_i^\pi \rightarrow J_f^\pi$
Band Q6					
802.2	11390				$26^{(-)} \rightarrow 24^{(-)}$
287.1	10587				$24^{(-)} \rightarrow 24^{(-)}$
325.4	11390		0.30(5)	$M1/E2$	$26^{(-)} \rightarrow 26^{(-)}$
1026.5	10587		0.68(4)	$E2$	$24^{(-)} \rightarrow 22^{(-)}$
Band Q7					
679.0	12516	3.6	0.60(9)	$E2$	$29^{(-)} \rightarrow 27^{(-)}$
1057.2	13573	4.1	0.74(7)	$E2$	$31^{(-)} \rightarrow 29^{(-)}$
1319.5	14892	1.4	0.72(15)	$E2$	$33^{(-)} \rightarrow 31^{(-)}$
1438.3	16330	0.5			$(35^-) \rightarrow 33^{(-)}$
400.9	12516	0.3			$29^{(-)} \rightarrow 28^{(-)}$
447.2	11837	0.3	0.27(3)	$M1/E2$	$27^{(-)} \rightarrow 26^{(-)}$
772.9	11837	2.7	0.38(10)	$M1/E2$	$27^{(-)} \rightarrow 26^{(-)}$
Band Q8					
930.5	14399				$(32^+) \rightarrow (30^+)$
1193.5	15592			$(E2)$	$(34^+) \rightarrow (32^+)$
1288.3	16881				$(36^+) \rightarrow (34^+)$
826.4	14399				$(32^+) \rightarrow 31^{(-)}$
952.9	13468				$(30^+) \rightarrow 29^{(-)}$
Band Q9					
809.1	13041	11.0	0.66(3)	$E2$	$30^{(+)} \rightarrow 28^{(+)}$
908.4	13949	9.6	0.71(4)	$E2$	$32^{(+)} \rightarrow 30^{(+)}$
1081.1	15031	7.7	0.75(8)	$E2$	$34^{(+)} \rightarrow 32^{(+)}$
1395.6	16427		0.83(17)	$E2$	$36^{(+)} \rightarrow 34^{(+)}$
1440.9	17868				$(38^+) \rightarrow 36^{(+)}$
675.8	12232	1.9	0.65(7)	$E2$	$28^{(+)} \rightarrow 26^+$
875.0	12232	4.1	0.37(4)	$E1$	$28^{(+)} \rightarrow 27^{(-)}$
1234.5	16265		0.67(10)	$E2$	$36^{(+)} \rightarrow 34^{(+)}$
Band Q10					
779.1	15015		0.73(11)	$E2$	$(33^-) \rightarrow (31^-)$
1059.4	16075		0.77(12)	$E2$	$(35^-) \rightarrow (33^-)$
1318.5	17393		0.79(16)	$E2$	$(37^-) \rightarrow (35^-)$
1542.6	18936			$(E2)$	$(39^-) \rightarrow (37^-)$
476.9	14236				$(31^-) \rightarrow (30^-)$
788.5	15015		0.63(10)	$E2$	$(33^-) \rightarrow (31^-)$
910.5	14236		0.64(5)	$E2$	$(31^-) \rightarrow (29^-)$
Band Q11					
894.2	16024	0.8	0.50(20)	$E2$	$(35^-) \rightarrow (33^-)$
1042.3	17066	0.8	0.59(6)	$E2$	$(37^-) \rightarrow (35^-)$
1239.5	18305	1.1	0.76(15)	$E2$	$(39^-) \rightarrow (37^-)$
1381.8	19687	1.1			$(41^-) \rightarrow (39^-)$
1513.4	21201	1.1			$(43^-) \rightarrow (41^-)$
1665.6	22867	0.5			$(45^-) \rightarrow (43^-)$
1829.3	24696	0.3			$(47^-) \rightarrow (45^-)$
1975.4	26671	0.1			$(49^-) \rightarrow (47^-)$
888.8	16024	0.7			$(35^-) \rightarrow (33^-)$
1436.2	15129	1.4			$(33^-) \rightarrow 31^{(-)}$
1008.3	16024		0.71(10)	$E2$	$(35^-) \rightarrow (33^-)$
Band Q12					
913.4	13384	1.0			$(31^+) \rightarrow (29^+)$
1078.6	14463	2.2	0.57(14)	$E2$	$(33^+) \rightarrow (31^+)$
1250.7	15713	2.2	0.66(8)	$E2$	$(35^+) \rightarrow (33^+)$
1426.5	17140	1.6			$(37^+) \rightarrow (35^+)$
1571.4	18711	1.1			$(39^+) \rightarrow (37^+)$

TABLE I. (*Continued*.)

γ-ray energy[a]	E_i (keV)	Intensity[b]	Anisotropy[c]	Multipolarity	$J_i^\pi \rightarrow J_f^\pi$
1704.0	20415	0.5			$(41^+) \rightarrow (39^+)$
1859.5	22275	0.3			$(43^+) \rightarrow (41^+)$
2010.2	24285	0.1			$(45^+) \rightarrow (43^+)$
971.2	13384	0.8			$(31^+) \rightarrow 29^{(-)}$
1114.4	12471	0.05			$(29^+) \rightarrow 27^{(-)}$
Band D1					
195.9	6179		0.36(11)	$M1/E2$	$(16^-) \rightarrow (15^-)$
249.0	6428				$(17^-) \rightarrow (16^-)$
313.2	6741		0.37(4)	$M1/E2$	$(18^-) \rightarrow (17^-)$
424.3	7165		0.29(5)	$M1/E2$	$(19^-) \rightarrow (18^-)$
1283.1	5983				$(15^-) \rightarrow 13^-$
Band D2					
150.2	7201		0.35(7)	$M1/E2$	$18^- \rightarrow 17^-$
280.6	7482		0.26(4)	$M1/E2$	$19^- \rightarrow 18^-$
551.8	8034				$(20^-) \rightarrow 19^-$
240.2	7201		0.31(4)	$M1/E2$	$18^- \rightarrow 17^-$
1441.3	7051		0.61(10)	$E2$	$17^- \rightarrow 15^-$
Band D3					
144.7	8770		0.23(15)	$M1/E2$	$22^- \rightarrow 21^-$
233.4	9004		0.33(5)	$M1/E2$	$23^- \rightarrow 22^-$
252.2	8770		0.27(3)	$M1/E2$	$22^- \rightarrow 21^-$
442.0	8625		0.34(5)	$M1/E2$	$21^- \rightarrow 20^-$
1195.7	8625			$(E1)$	$21^- \rightarrow 20^+$
Band D4					
154.7	7943		0.33(5)	$M1/E2$	$19^- \rightarrow 18^-$
240.6	8184		0.25(6)	$M1/E2$	$20^- \rightarrow 19^-$
334.3	8518		0.35(5)	$M1/E2$	$21^- \rightarrow 20^-$
485.9	9004		0.35(14)	$M1/E2$	$22^- \rightarrow 21^-$
512.5	9517		0.26(4)	$M1/E2$	$23^- \rightarrow 22^-$
477.5	9994		0.25(7)	$M1/E2$	$24^- \rightarrow 23^-$
312.0	9316		0.36(7)	$M1/E2$	$23^- \rightarrow 22^-$
447.5	9763		0.31(5)	$M1/E2$	$24^- \rightarrow 23^-$
755.1	8184		0.68(8)	$M1/E2$	$20^- \rightarrow 20^+$
1386.5	7789				$18^- \rightarrow 17^-$
1541.2	1943		0.84(20)	$E2$	$19^- \rightarrow 17^-$
Band D5					
160.5	6887		0.26(2)	$M1/E2$	$16^+ \rightarrow 15^+$
240.6	7127		0.25(5)	$M1/E2$	$17^+ \rightarrow 16^+$
392.1	7519		0.27(4)	$M1/E2$	$18^+ \rightarrow 17^+$
523.0	8042		0.29(5)	$M1/E2$	$19^+ \rightarrow 18^+$
215.3	6726				$15^+ \rightarrow (14^+)$
271.6	7127				$17^+ \rightarrow 16^+$
325.3	7127		0.21(3)	$M1/E2$	$17^+ \rightarrow 16^+$
362.1	7127		0.21(3)	$M1/E2$	$17^+ \rightarrow 16^+$
379.2	6726		0.23(5)	$M1/E2$	$15^+ \rightarrow 15^{(+)}$
385.2	6347		0.34(4)	$(E1)$	$15^{(+)} \rightarrow (14^-)$
418.2	6765		0.31(5)	$M1/E2$	$16^{(+)} \rightarrow 15^{(+)}$
455.5	6802		0.23(3)	$M1/E2$	$16^+ \rightarrow 15^{(+)}$
509.4	6856		0.30(2)	$M1/E2$	$16^+ \rightarrow 15^{(+)}$
540.0	6887		$<$0.4	$M1/E2$	$16^+ \rightarrow 15^{(+)}$
548.0	6511		0.67(15)	$M1/E2$	$(14^+) \rightarrow 14^+$
558.1	7519				$18^+ \rightarrow 17^-$
867.2	5963				$(14^-) \rightarrow 12^-$
1117.1	7519				$18^+ \rightarrow 17^-$

TABLE I. (*Continued*.)

γ-ray energy[a]	E_i (keV)	Intensity[b]	Anisotropy[c]	Multipolarity	$J_i^\pi \rightarrow J_f^\pi$
1155.6	6765				$16^+ \rightarrow 15^-$
1217.1	6856				$16^+ \rightarrow 15^-$
1246.3	6856				$16^+ \rightarrow 15^-$
1338.2	6765				$16^+ \rightarrow 14^-$
1366.3	7519		0.60(8)	$E2$	$18^+ \rightarrow 16^+$
Band D6					
356.6	8899		0.38(12)	$M1/E2$	$21^+ \rightarrow 20^+$
440.8	9340		0.30(4)	$M1/E2$	$22^+ \rightarrow 21^+$
524.1	9864		0.27(7)	$M1/E2$	$23^+ \rightarrow 22^+$
599.2	10464		0.26(4)	$M1/E2$	$24^+ \rightarrow 23^+$
500.4	8543		0.34(10)	$M1/E2$	$20^+ \rightarrow 19^+$
1023.5	8543				$20^+ \rightarrow 18^+$
Band D7					
154.2	8317		0.33(5)	$M1/E2$	$19^{(+)} \rightarrow 18^{(+)}$
282.0	8599		0.24(2)	$M1/E2$	$20^{(+)} \rightarrow 19^{(+)}$
429.5	9028		0.23(5)	$M1/E2$	$21^{(+)} \rightarrow 20^{(+)}$
531.3	9559		0.24(7)	$M1/E2$	$22^{(+)} \rightarrow 21^{(+)}$
485.9	9028		0.33(2)	$M1/E2$	$21^{(+)} \rightarrow 20^+$
555.9	8599		0.40(6)	$M1/E2$	$20^{(+)} \rightarrow 19^+$
659.9	9559				$22^{(+)} \rightarrow 21^+$
797.1	8317		0.30(5)	$M1/E2$	$19^{(+)} \rightarrow 18^+$
1035.3	8163				$18^{(+)} \rightarrow 17^+$
Band D8					
221.6	9885		0.31(5)	$M1/E2$	$23^{(-)} \rightarrow 22^{(-)}$
370.7	10256		0.32(5)	$M1/E2$	$24^{(-)} \rightarrow 23^{(-)}$
477.4	10733		0.37(7)	$M1/E2$	$25^{(-)} \rightarrow 24^{(-)}$
571.2	11304		0.36(5)	$M1/E2$	$26^{(-)} \rightarrow 25^{(-)}$
653.2	11957		0.29(4)	$M1/E2$	$27^{(-)} \rightarrow 26^{(-)}$
325.7	9885		0.29(5)	$M1/E2$	$23^{(-)} \rightarrow 22^{(+)}$
544.7	9885		0.32(3)	$M1/E2$	$23^{(-)} \rightarrow 22^+$
636.0	9664		0.29(5)	$M1/E2$	$22^{(-)} \rightarrow 21^{(+)}$
Band D9					
424.7	13314		0.23(15)	$M1/E2$	$(30^+) \rightarrow (29^+)$
451.9	12889		0.29(4)	$M1/E2$	$(29^+) \rightarrow (28^+)$
591.9	13906		0.27(4)	$M1/E2$	$(31^+) \rightarrow (30^+)$
791.9	14698				$(32^+) \rightarrow (31^+)$
877.0	13314		0.54(8)	$E2$	$(30^+) \rightarrow (28^+)$
472.0	12889		0.26(3)	$M1/E2$	$(29^+) \rightarrow (28^+)$
1251.7	12417				$(28^+) \rightarrow 26^+$
1270.8	12437	1.9			$(28^+) \rightarrow 26^+$
Band D10					
245.4	12184		0.33(6)	$M1/E2$	$(26^-) \rightarrow (25^-)$
354.3	12539			$(M1/E2)$	$(27^-) \rightarrow (26^-)$
368.9	12908		0.34(15)	$M1/E2$	$(28^-) \rightarrow (27^-)$
417.5	13325		0.26(7)	$M1/E2$	$(29^-) \rightarrow (28^-)$
433.3	13758		<0.4	$M1/E2$	$(30^-) \rightarrow (29^-)$
468.9	14227		0.31(10)	$M1/E2$	$(31^-) \rightarrow (30^-)$
522.3	14750				$(32^-) \rightarrow (31^-)$
577.7	15327			$(M1/E2)$	$(33^-) \rightarrow (32^-)$
599.1	12539				$(27^-) \rightarrow (25^-)$
653.2	15981		<0.4	$M1/E2$	$(34^-) \rightarrow (33^-)$
723.3	12908				$(28^-) \rightarrow (26^-)$
786.8	13325		0.64(14)	$E2$	$(29^-) \rightarrow (27^-)$
850.5	13758		0.54(10)	$E2$	$(30^-) \rightarrow (28^-)$
901.9	14227		0.63(15)	$E2$	$(31^-) \rightarrow (29^-)$

TABLE I. (*Continued*.)

γ-ray energy[a]	E_i (keV)	Intensity[b]	Anisotropy[c]	Multipolarity	$J_i^\pi \rightarrow J_f^\pi$
992.3	14750				$(32^-) \rightarrow (30^-)$
1100.3	15327				$(33^-) \rightarrow (31^-)$
1231.7	15981				$(34^-) \rightarrow (32^-)$
287.4	12227				$(26^-) \rightarrow (25^-)$
312.2	12539		0.27(6)	$M1/E2$	$(27^-) \rightarrow (26^-)$
514.1	14750				$(32^-) \rightarrow (31^-)$
680.3	12908				$(28^-) \rightarrow (26^-)$
Band D11					
285.5	14529				$31^{(-)} \rightarrow (30^-)$
317.2	14846		0.25(3)	$M1/E2$	$32^{(-)} \rightarrow 31^{(-)}$
457.2	15303				$33^{(-)} \rightarrow 32^{(-)}$
458.2	15762		0.34(10)	$M1/E2$	$34^{(-)} \rightarrow 33^{(-)}$
511.7	16274		0.33(5)	$M1/E2$	$35^{(-)} \rightarrow 34^{(-)}$
603	14846				$32^{(-)} \rightarrow (30^-)$
690.1	16963		<0.4	$(M1/E2)$	$36^{(-)} \rightarrow 35^{(-)}$
702.8	17665	0.3	0.34(10)	$M1/E2$	$37^{(-)} \rightarrow 36^{(-)}$
774.4	15303				$33^{(-)} \rightarrow 31^{(-)}$
793	18458				$38^{(-)} \rightarrow 37^{(-)}$
915.2	15762				$34^{(-)} \rightarrow 32^{(-)}$
970.6	16274			$(E2)$	$35^{(-)} \rightarrow 33^{(-)}$
1201.3	16963				$36^{(-)} \rightarrow 34^{(-)}$
1393	17665	0.7	0.65(10)	$E2$	$37^{(-)} \rightarrow 35^{(-)}$
1496	18458				$(38^-) \rightarrow 36^{(-)}$
536	16963				$36^{(-)} \rightarrow 36^{(-)}$
730.6	15762				$34^{(-)} \rightarrow 33^{(-)}$
897.3	14846				$32^{(-)} \rightarrow 32^{(-)}$
1203.1	14244				$(30^-) \rightarrow 30^{(-)}$
1238	17665				$39^{(-)} \rightarrow 36^{(-)}$
1243.5	16274	3.3	0.38(8)	$M1/E2$	$35^{(-)} \rightarrow 34^{(-)}$
1273.8	14846				$32^{(-)} \rightarrow 31^{(-)}$
1354.0	15303				$33^{(-)} \rightarrow 32^{(-)}$
1488	14529				$(31^-) \rightarrow 30^{(-)}$

[a]The error on the transition energies is 0.2 keV for transitions below 1000 keV and intensities larger than 5% of the ^{140}Nd reaction channel, 0.5 keV for transitions above 1000 keV and intensities lower than 5%, and 1 keV for transitions above 1200 keV and/or weaker than 1%.

[b]Relative intensities corrected for efficiency. The transition intensities were obtained from a combination of total projection and gated spectra.

[c]The anisotropy has been deduced from two asymmetric γ-γ coincidence matrices sorted with all detectors on one axis and detectors at 90° and at forward/backward angles, respectively, on the other axis. The tentative spin-parity of the states are given in parenthesis.

two new bands Q2 and Q4 which decay towards Q1 and Q3, respectively. We confirm all previously identified transitions of bands Q1, Q2, and Q3. The new weakly populated band Q4 decays only towards Q3.

The transitions populating higher-lying states of band Q9 which were previously drawn as non-yrast sequences are now ordered and placed in the newly identified dipole band D11. The 1234, 1368, 1509 keV cascade is not confirmed. The 1396 and 1441 keV transitions are now included in band Q9, while the 457, 458, 690, 703, 897, 1354, and 1391 keV transitions are included in band D11 or in its decay towards band Q9.

Band Q10 has been identified previously and it was clear that it decays through a structure like a dipole band with crossover transitions. The JUROGAM II experiment was again very helpful in understanding the structure of this band and its decay. In fact, we observed the transitions of bands Q10 and D10 in the spectra gated by low-lying transitions of ^{140}Nd observed at the focal plane of RITU, which indicates that the bands have a delayed decay component. We have accurately searched for the transitions linking D10 to the 20^+ isomer, but we could not find any.

We have instead identified a new $E2$ transition of 1008 keV which links band Q11 to Q10, which fixes the excitation energy and spin-parity of bands Q10 and D10, since Q11 is linked to band Q3 and therefore its excitation energy and spins are known. The existence of the 1008 keV transition can be understood through the mixing of the 35^+ states of the bands Q10 and Q11, which are separated by only 51 keV.

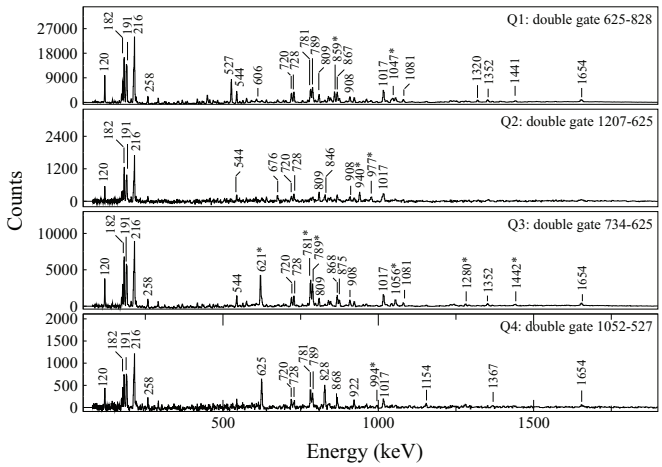

FIG. 2. Double-gated spectra for bands Q1–Q4 in ^{140}Nd. The gates were set on selected transitions of each band. The transitions marked with asterisks represent the members of the band.

However, the decay of band D10 remains unknown. It can be that due to the high excitation energy of the band the decay is fragmented. Moreover, one cannot exclude the possible existence of another unidentified isomeric state to which band D10 decays.

The band Q5 was observed previously and linked to low-lying states. We confirm all previously identified transitions and extend it at the bottom by two more states populated and deexcited by the 868 and 1566 keV transitions, respectively. Four new transitions with energies of 415, 533, 543, and 932 keV link band Q5 to bands D8, D7, Q1, and D5, respectively.

Band Q6 is new. It consists of only two states linked by the 803 keV transition and decays towards band Q5 through the 287, 326, and 1026 keV transitions.

Band Q7 was observed previously and its transitions and decay-out are confirmed. The 1274 keV transition linking band D11 to the 31^+ state of band Q7 is also confirmed, giving

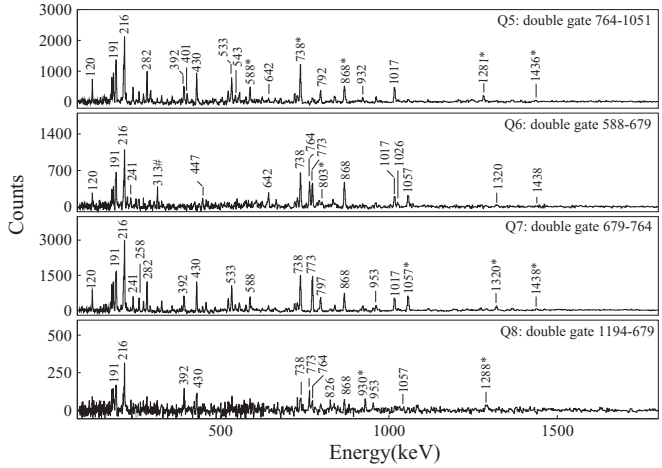

FIG. 3. Double-gated spectra for the bands Q5–Q8 in ^{140}Nd. The gates were set on selected transitions of each band. The transitions marked with asterisks represent the members of the band, while the peaks marked with a # are contaminants from other nuclei.

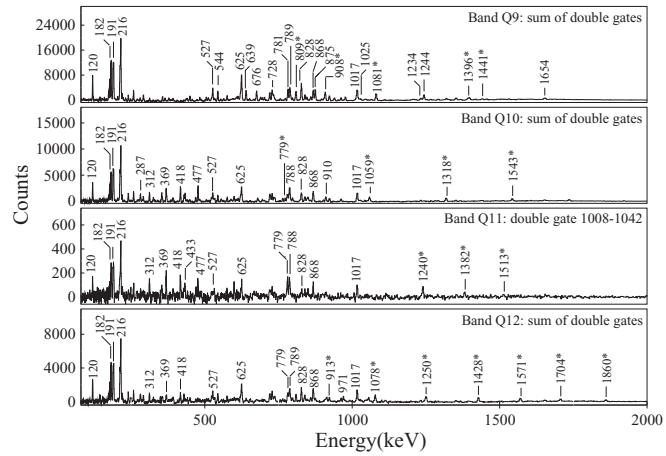

FIG. 4. Double-gated spectra for the bands Q9–Q12 in ^{140}Nd. The gates were set on selected transitions of each band. The transitions marked with asterisks represent the members of the band.

additional confidence in the spin-parity assignment to the high-spin bands.

Band Q8 is new. It decays to band Q7 through the 826 and 953 keV transitions.

1. The dipole bands (D1–D11)

Spectra obtained by doubly gating on selected transitions of the different D bands are shown in Figs. 5–7.

Most of the transitions in these spectra were observed in prompt coincidence with both the EUROBALL and JUROGAM II arrays. The use of the recoil tagging technique in the JUROGAM II experiment allowed the observation of very weak transitions populating the 20^+ isomer. The results of this experiment have been published in a separate paper [10].

Band D1 is new. It is weakly populated and decays through the 1283 keV $\Delta I = 2$ transition to the 13^- state. We chose the $E2$ character for the 1283 keV transition which leads to a negative-parity assignment for the states of band D1, since in

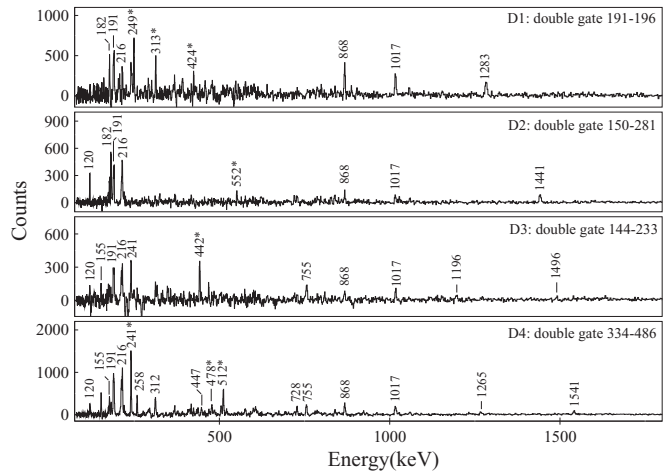

FIG. 5. Double-gated spectra for bands D1–D4 in ^{140}Nd. The gates were set on selected transitions of each band. The transitions marked with asterisks represent the members of the band.

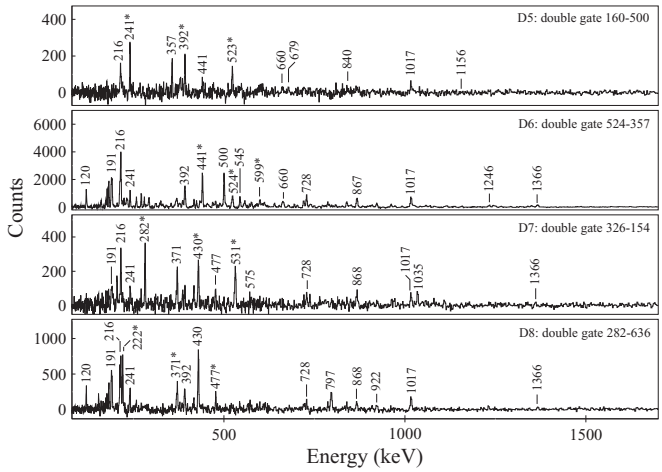

FIG. 6. Double-gated spectra for the bands D5-D8 in ^{140}Nd. The gates were set on selected transitions of each band. The transitions marked with asterisks represent the members of the band.

this case the decay of the 20^+ isomer to the 18^- state of band D1 is inhibited, as it should be.

Band D2 was observed previously, but with the 240 keV transition considered in band and the 150 keV transition out of band. We now invert the two transitions, since the 17^- state populated by 240 keV is clearly a state on its own, to which many other bands decay, while the 17^- state populated by 150 keV is only populated by the 281 keV transition of band D2.

Band D3 was observed previously. The high sensitivity of the JUROGAM II experiment allowed the identification of one new in-band transition of 233 keV and two new decay transitions of 252 and 1196 key towards band D4 and the 20^+ isomer, respectively.

Band D4 was observed previously. We identified two new in-band transitions of 155 and 478 keV, and two new decay transitions of 755 and 1386 keV towards the 20^+ isomer and the yrast 17^- state, respectively. At the top of the band we also identified two dipole transitions of 312 and 448 keV, which are placed in parallel with the 512–478 keV cascade.

Band D5 is new, in the sense that previously observed transitions which were placed in the level scheme without emphasizing a band structure are now grouped in a sequence of dipole transitions with energies ranging from 161 to 523 keV. Several new transitions were placed at the bottom of the band (215, 325, 418, 456, 509, 540, 548, 867, 1156). The decay of the band is fragmented and occurs from the four lowest-lying states to the negative-parity states below the 20^+ isomer.

Band D6 has been observed previously. We add one more transition of 599 keV at the top and one of 1024 keV deexciting it towards band D5.

Band D7 is also new, in the sense that previously observed transitions were grouped to form a band of dipole transitions. In addition to the previously observed transition we identified one transition of 154 keV at the bottom of the band and several decay transitions towards bands D5 and D6 (486, 660, 1035 keV).

Band D8 was observed previously and is confirmed. We identified one new decay transition of 545 keV towards band D6.

Band D9 is new. It is composed of transitions previously observed and placed on top of band Q1. We have now draw the observed states differently and add two new transitions of 592 and 792 keV on top of the band and one crossover transition of 877 keV.

Band D10 is new. It consists of the transitions which were previously placed at the bottom of band Q10, to which we add many newly identified transitions: 245, 287, 522, 578, 599, 653, 680, 992, 1100, 1232 keV. However, as discussed in the previous subsection, the decay of band D10 to low-lying states is not established. It is clear that it decays to one or more isomeric states since we see the transitions of band D10 in coincidence with the low-lying transitions of ^{140}Nd observed at the focal plane of RITU, but the band can also have prompt decay branches.

Band D11 is the highest excited dipole band and is composed of transitions that were not grouped in bands previously (see the discussion of band Q9). Many new transitions have been identified and put together to form a dipole band with crossover transitions, which decays towards Q9. Band D11 is also connected to band Q7 by the 1274 keV transition.

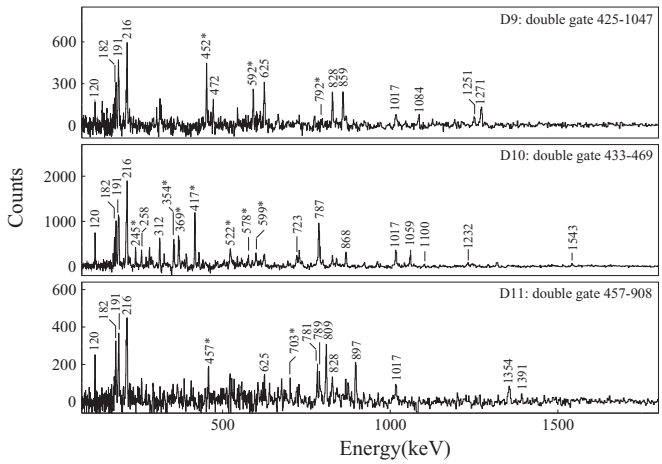

FIG. 7. Double-gated spectra for the bands D9, D10, D11 in ^{140}Nd. The gates were set on selected transitions of each band. The transitions marked with asterisks represent the members of the band.

IV. DISCUSSION

The level structure of ^{140}Nd with 60 protons and 80 neutrons can be considered to arise from an interaction between 10 proton particles on top of the $Z = 50$ major shell and 2 neutron holes in the $N = 82$ major shell. In the low-energy regime, the nucleus is expected to have a small deformation, $\epsilon_2 \sim 0.1$–0.2. Thus it is convenient to express the single-particle states in terms of j-shell quantum numbers. The lowest proton configuration has four protons holes in the $\pi g_{7/2}$, $\pi d_{5/2}$ orbitals which interact and are strongly mixed. Higher angular momenta from proton configurations can be obtained by exciting one or two protons from $\pi g_{7/2}$, $\pi d_{5/2}$ to $\pi h_{11/2}$. The lowest neutron configuration has two holes

in the $\nu d_{3/2}$, $\nu s_{1/2}$ orbitals which interact and are strongly mixed. Higher angular momenta from neutron configurations can be obtained by exciting one or two neutrons from the $\nu h_{11/2}$ orbital into the $\nu d_{3/2}$, $\nu s_{1/2}$ orbitals, all lying below the $N = 82$ shell gap. Higher excited states and angular momenta can be obtained from neutron excitations above the $N = 82$ shell gap into the $\nu f_{7/2}$, $\nu h_{9/2}$, and $\nu i_{13/2}$ orbitals.

The level structure of ^{140}Nd at low spins has been well described within the CNS model as built on spherical configurations up to the 20^+ isomer [8], which was interpreted as a maximum aligned configuration with four proton holes in the $\pi(dg)$ subshell and two neutron holes in the $\nu h_{11/2}$ subshell, i.e., a $\pi(dg)^4 \otimes \nu h^2$ configuration. The new bands observed at medium and high spins are sequences of either quadrupole or dipole transitions, which we labeled as Q and D bands, and will be discussed separately using the CNS and the TAC models, respectively.

A. The cranked Nilsson-Strutinsky (CNS) formalism

The Q bands will be analyzed using the cranked Nilsson-Strutinsky (CNS) formalism [21–23]. This formalism is based on the Nilsson or modified oscillator potential, where the total energy is obtained as a sum of the rotating liquid drop energy and the shell energy [23,24]. This energy is calculated in a mesh of deformations ε_2, γ, and ε_4, and the minimum is searched as a function of these parameters. In the calculations of the single-particle energies, we have used the so-called $A = 150$ parameters [25], which are known to give a good description of the low-deformation configurations of nuclei with a few particles outside the ^{146}Gd core; see, e.g., [26] and references therein. By introducing some minor approximations which are essentially negligible at the small deformations of the triaxial ^{140}Nd bands, it becomes possible to label the orbitals as belonging to a specific $\mathcal{N}$ shell and as being of high-j (intruder) or low-j character. These labels are applicable in the full deformation space, which makes it possible to specify the configurations of the triaxial bands in Nd nuclei with $N \approx 78$–80 relative to a ^{132}Sn core as

$$\begin{aligned} &\pi\left[(d_{5/2}g_{7/2})^{p_1}_{\alpha_1}(h_{11/2})^{p_2}_{\alpha_2}\right], \\ &\nu\left[(d_{3/2}s_{1/2})^{-n_1}_{\alpha_3}(h_{11/2})^{-n_2}_{\alpha_4}(h_{9/2}f_{7/2})^{n_3}_{\alpha_5}(i_{13/2})^{n_4}_{\alpha_6}\right], \end{aligned} \tag{1}$$

defining the number of particles and holes in the different groups of orbitals. In addition, signature α is a preserved quantum number which can be specified for each orbital and thus also for the different groups in Eq. (1). For an odd number of particles or holes, α takes the values $+1/2$ or $-1/2$, while for the low-lying configurations $\alpha = 0$ for an even number of particles. With no loss of information we can use the condensed configuration labels

$$\left[(p_1)_{\alpha_1}(p_2)_{\alpha_2}, (n_1)_{\alpha_3}(n_2)_{\alpha_4}(n_3)_{\alpha_5}(n_4)_{\alpha_6}\right]. \tag{2}$$

In these labels, the signature α will be written as $\pm$ for an odd number of particles while $\alpha = 0$ for an even number of particles will not be specified. Furthermore, if α is not specified for a small number of odd particles in a high-j shell, it is assumed that it takes the favored value, $\alpha = 1/2$ for even $\mathcal{N}$ and $\alpha = -1/2$ for odd $\mathcal{N}$. In order to distinguish the large number of calculated bands in ^{140}Nd, we will use the labeling in Eq. (2), which is more complete than $[p_2, n_2(n_3n_4)]$ which has been used in previous studies of the triaxial bands in $^{138-140}$Nd [2,3,6]. The new feature to specify the signature in the CNS labels has been introduced in a less systematic way previously; see, e.g., [27–30].

B. CNS analysis of high-spin bands in ^{140}Nd

Calculated potential energy surfaces in the spin range $I = 24$–48 are shown in Fig. 8. There are essentially three different structures which are seen as different minima. The configurations close to spherical shape with no particles excited across the $N = 82$ gap are lowest in energy up to $I \approx 40$. For example the favored termination predicted for $I = 32$ [8] is seen as a well developed minimum at $\varepsilon_2 \approx 0.2$ and $\gamma \approx 30^\circ$. The triaxial minimum at $\varepsilon_2 = 0.20$–0.25, $\gamma = 30^\circ$–35° starts to develop around $I = 20$ and becomes yrast around $I = 40$. Finally, the superdeformed minimum [4] at $\varepsilon_2 \approx 0.45$, $\gamma \approx 0^\circ$ is seen for essentially all spin values but it becomes lowest in energy first for spin values close to $60\hbar$. The calculated deformation of the different triaxial high-spin configurations are rather stable, with $\varepsilon_2 \approx 0.20$, $\gamma \approx 32^\circ$, and $\varepsilon_4 \approx 0.01$ in the $I = 20$–30 spin range. In Fig. 9 we show two energy surfaces for the [82,22(20)] configuration assigned to band Q1 for spins $I = 18$ and $I = 24$, which shows a minimum at the same deformation as the minimum calculated for $(\pi = +, \alpha = 0)$ for $I = 24$ shown in Fig. 8.

The single-particle Routhians at this deformation are drawn in Fig. 10 as functions of the rotational frequency ω. Then in Fig. 11 we illustrate how the spin is built in the [82,22(20)] configuration which is assigned to the Q1 band; see below. There are four high-j particles which are almost fully aligned at $\omega = 0$, namely two $h_{11/2}$ protons and two $h_{9/2}f_{7/2}$ neutrons. The spin contribution from these particles at $\omega = 0$ is $\sim 16.3\hbar$ which comes rather close to the maximum value of $18\hbar$. These values are consistent with the fact that the Q1 band has not been observed below $I = 18\hbar$. With increasing rotational frequencies, the (dg) protons and $h_{11/2}$ neutrons contribute about equally to the spin while the contribution from the holes in the $(sd)_3$ neutron orbital at the top of the $\mathcal{N} = 4$ shell is negligible. In the $\mathcal{N} = 4$ proton orbitals, a crossing is formed at $\omega/\omega_0 \approx 0.07$ between the $\alpha = 1/2$ branches of the $(dg)_4$ and $(dg)_5$ orbitals. In Fig. 11 we have followed the $(dg)_4$ orbital through the crossing, which leads to a smooth development of the spin contribution for the (dg) particles. In the CNS calculations, for configurations with four $\alpha = 1/2$ (dg) protons, the lowest four orbitals of this type are occupied, i.e., the $(dg)_4$ orbital is occupied at low frequencies and the $(dg)_5$ orbital at high frequencies. This leads to a discontinuity in the spin contribution and then also in the E-vs-I curves. Such discontinuities are seen in some of the calculated bands discussed below.

From the single-particle orbitals in Fig. 10 we can get a good idea about which are the important configurations for the building of triaxial bands. There are only three important proton configurations which have two or three $h_{11/2}$ particles. They can be combined with a large number of neutron configurations. We have thus mainly considered the favored

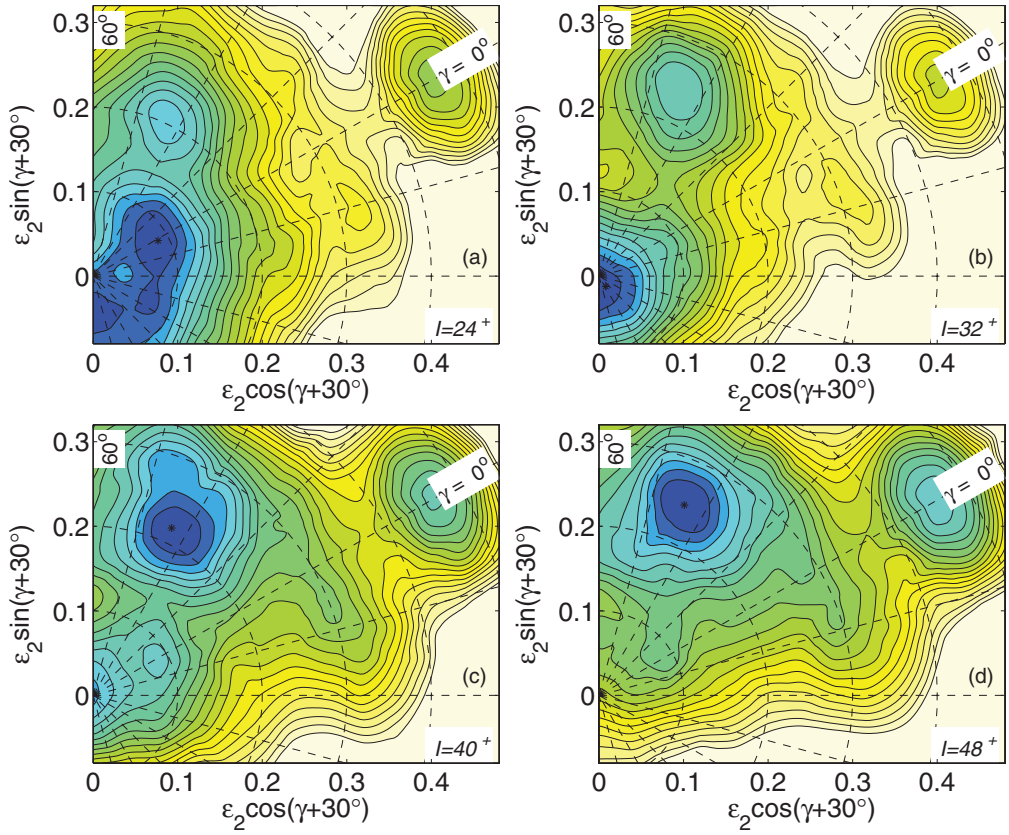

FIG. 8. (Color online) Calculated potential energy surfaces in the (ε_2, γ) plane for ^{140}Nd, with fixed parity and signature ($\pi = +,\ \alpha = 0$), in the spin range relevant for the observed high-spin bands ($I = 24^+, 32^+, 40^+, 48^+$). The contour line separation is 0.25 MeV.

configurations with one, two, or three neutrons in the three high-j orbitals which come in the region of the $N = 80$ Fermi level around $\omega/\omega_0 = 0.04$. The bands with negative parity and odd spin ($\alpha = 1$) resulting from these proton and neutron configurations are shown in Fig. 12. Such figures have also been produced for the other spin-parity combinations and examined in the process of configuration assignment. A typical feature of the triaxial bands is a parabola-like behavior of the $E - E_{rld}$ curves with a well defined minimum at some value of I. These are the bands of main interest here. Besides these bands, one notes that, for example, the bands with one $\mathcal{N} = 4$ neutron hole and one high-j neutron have a rather different behavior with terminating states which are not too far above yrast. For example, the $[7_+3, 1_+2(01)]$ configuration terminates at $I = 43^-$ in the state

$$\pi\left[(d_{5/2}g_{7/2})^7_{12.5}(h_{11/2})^3_{13.5}\right],$$
$$\nu\left[(d_{3/2}s_{1/2})^{-1}_{0.5}(h_{11/2})^{-2}_{10}(i_{13/2})^1_{6.5}\right],$$

where the total spin in the different groups is specified as a subscript. Some bands in Fig. 12 show band crossings, as most clearly seen at $I \approx 39$ in the $[82, 23_+(21)]$ configuration. This is caused by the unpaired band crossing between the $(dg)_4$ and $(dg)_5$ orbitals discussed above.

The $E - E_{rld}$ curves of the Q bands, which are observed in an extended spin range, are compared with the configurations assigned to them in Fig. 13. In general, the difference between experiment and calculations follows the expected trend. It is rather constant and close to zero above $I = 30$, while it increases towards lower spin values, suggesting that pairing starts to play a role. The Q11 and Q12 bands show the strange feature that the differences increase at the highest spin values, especially for Q11. It is also somewhat strange that the $[7_-3, 3_-2(21)]$ configuration is calculated to be so low in energy when compared with its experimental counterpart, Q11. An alternative assignment for the Q11 band is $[82, 3_-3_-(22)]$, i.e., a configuration with four high-j neutron particles. With

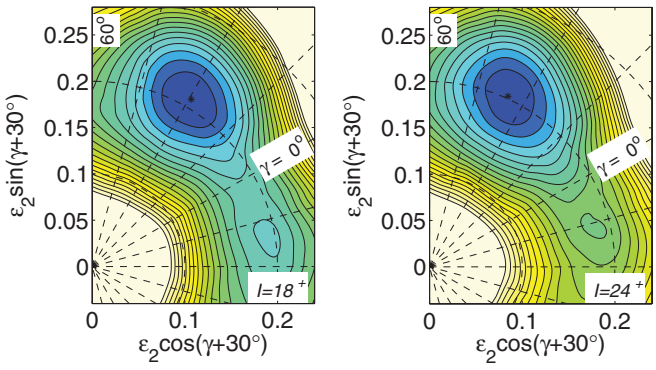

FIG. 9. (Color online) Calculated potential energy surfaces in the (ε_2, γ) plane for the [82,22(20)] configuration assigned to band Q1 of ^{140}Nd. The contour line separation is 0.25 MeV.

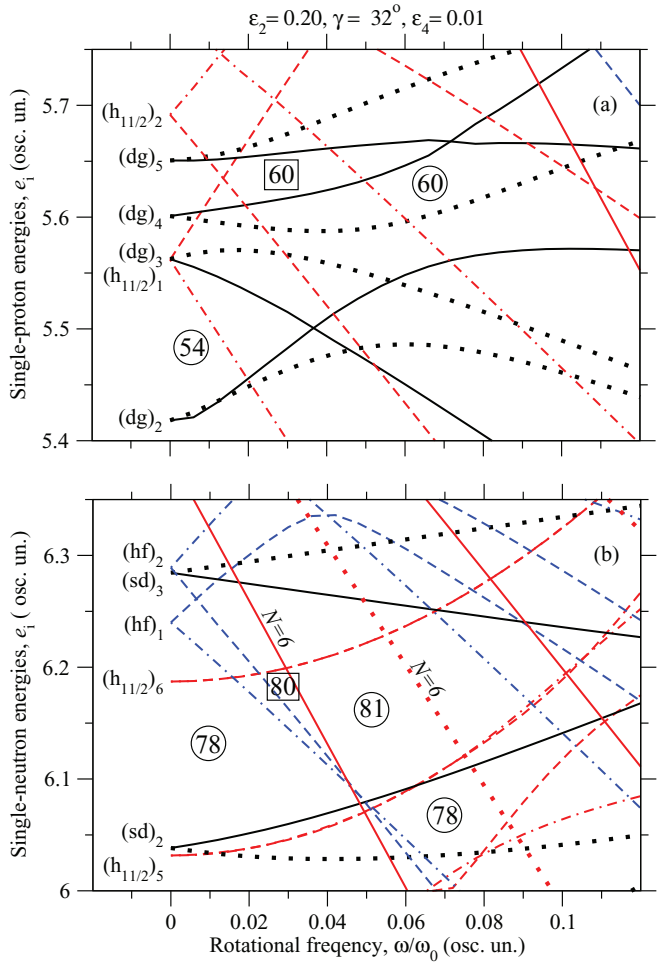

FIG. 10. (Color online) The calculated single-particle Routhians at an approximate deformation for the [82,22(20)] configuration drawn as functions of the rotational frequency. The gaps corresponding to this configuration are labeled by rectangles while some other particle numbers are given within circles. The orbitals are labeled by the subshells with the dominating amplitudes and by the ordering within the different groups. The proton $d_{5/2}g_{7/2}$ orbitals are labeled (dg) and the neutron $d_{3/2}s_{1/2}$ and $h_{9/2}f_{7/2}$ orbitals (sd) and (hf), respectively.

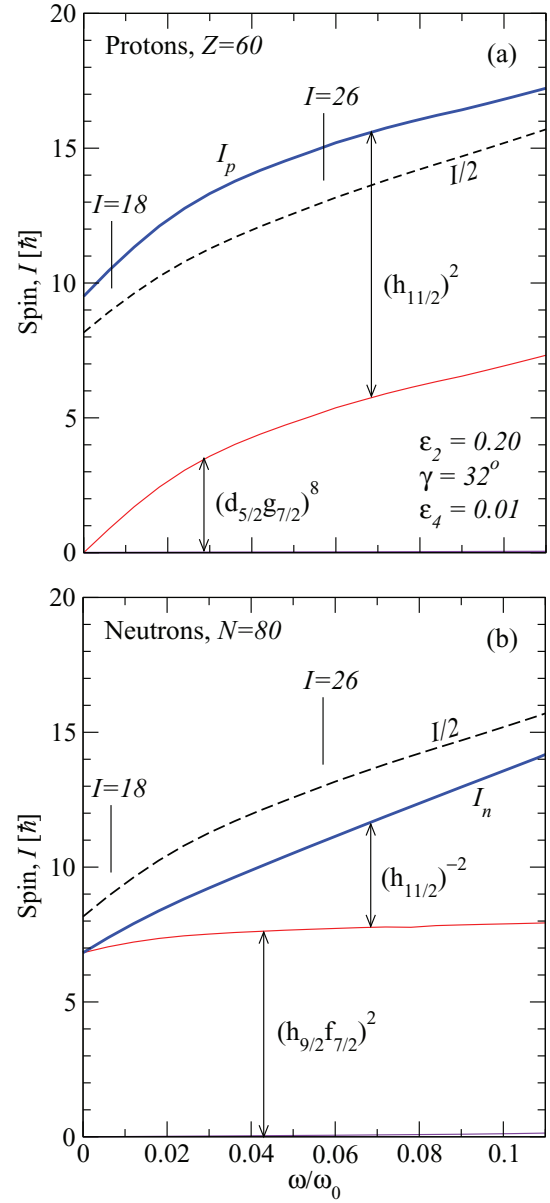

FIG. 11. (Color online) The spin contribution in the [82,22(20)] configuration from the different groups of orbitals drawn vs rotational frequency, ω. The total spin contribution from protons is labeled I_p and that from the neutrons I_n. The frequencies corresponding to the lowest and highest observed spin values in the [82,22(20)] configuration, $18\hbar$ and $26\hbar$, respectively, are indicated while the value of $I/2$ with $I = I_p + I_n$ is shown in both the proton and the neutron panels. The contribution from the $h_{11/2}$ neutrons, which is labeled $(h_{11/2})^{-2}$ is actually calculated as the contribution from the ten $h_{11/2}$ orbitals which are occupied. Note that the contributions from the proton and neutron cores and from the (sd) neutrons, which are drawn at the bottom of the respective diagrams, are essentially negligible.

this assignment, the energy agrees better with experiment but it is calculated to be too high for $I < 40$. Furthermore, such an assignment is not preferred because it would mean that the expected yrast band would not be observed, and that a band calculated to lie ∼1 MeV above the yrast line would be observed instead.

One of the criteria used to choose between the various possible configurations for a specific Q band was that the configurations of the band itself and the band towards which it decays are related by simple excitations. We have found that this criterium is in general fulfilled and understand the various connections between the bands as follows:

(i) The strongly populated Q3 band decays to the strongly populated Q1 band; [82, 22(1+1)] decays to [82,22(20)]; simple deexcitation of one neutron from $i_{13/2}$ to $(h_{9/2}f_{7/2})$.

(ii) The strongly populated Q9 band decays to the strongly populated Q3 band; [82, 3_2(21)] decays to [82, 22(1+1)]; simple deexcitation of one neutron from $(h_{9/2}f_{7/2})$ to (sd).

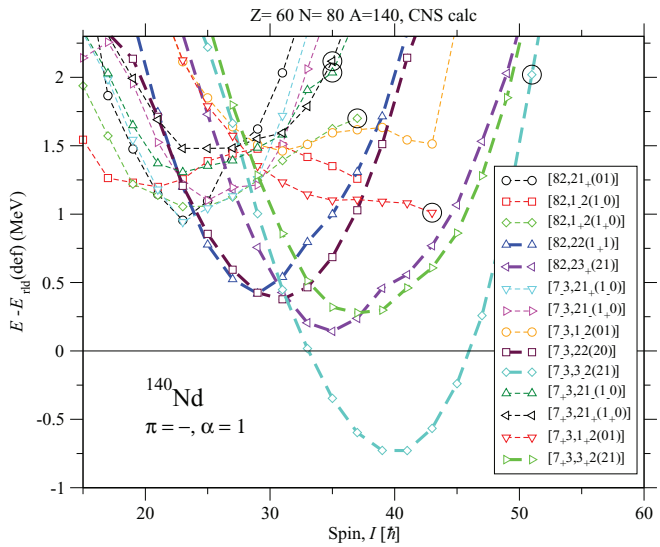

FIG. 12. (Color online) The configurations with negative parity and odd spin which result from the combination of the three proton configurations with two or three $h_{11/2}$ particles and 19 neutron configurations with up to three high-j particles are drawn relative to the rotating liquid drop energy. The bands which are assigned to an observed band are drawn with heavy lines. Noncollective aligned states are encircled.

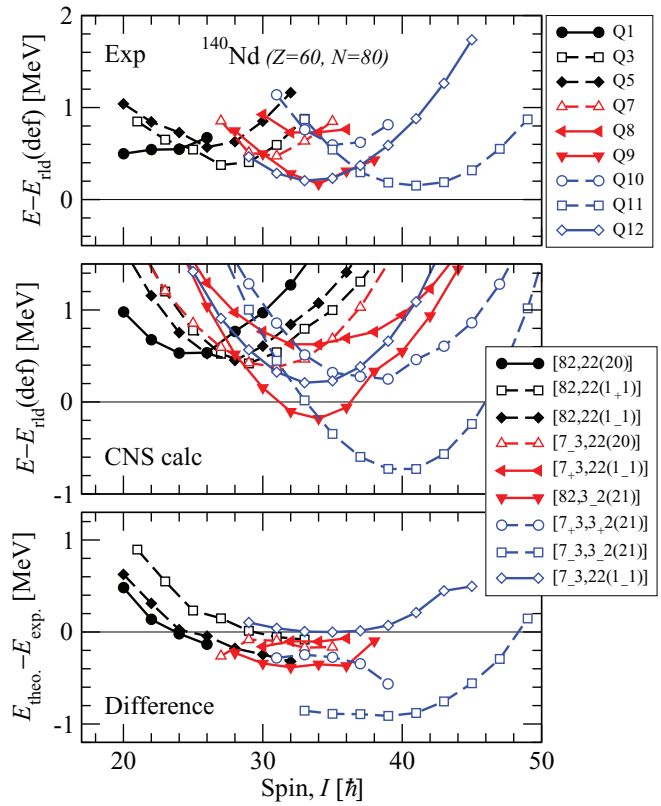

FIG. 13. (Color online) The observed Q bands in ^{140}Nd are shown relative to the rotating liquid drop energy in the upper panel, the calculated bands assigned to them are drawn in the middle panel, and the differences between experiment and calculations are presented in the bottom panel. The same types of lines and symbols are used for the related bands in the three panels.

(iii) Q12 decays to the strongly populated Q3 band; $[7_-3, 22(1_-1)]$ decays to $[82, 22(1_+1)]$; deexcitation of one proton from $h_{11/2}$ to (dg) and of one neutron from $(h_{9/2}f_{7/2})_{-1/2}$ to $(h_{9/2}f_{7/2})_{+1/2}$.

(iv) D11 decays to Q9; $[82, 23_\pm(21)]$ decays to $[82, 3_-2(21)]$; simple deexcitation of one neutron from $h_{11/2}$ to (sd).

(v) Q11 decays to Q3; $[7_-3, 3_-2(21)]$ decays to $[82, 22(1_+1)]$; deexcitation of one proton from $h_{11/2}$ to (dg) and of one neutron from $h_{9/2}f_{7/2}$ to (sd).

(vi) Q11 decays to Q10; $[7_-3, 3_-2(21)]$ decays to $[7_+3, 3_+2(21)]$; deexcitation of one proton from $(dg)_{-1/2}$ to $(dg)_{+1/2}$ and of one neutron from $(sd)_{-1/2}$ to $(sd)_{+1/2}$.

(vii) The band Q8 decays to Q7; $[7_+3, 22(1_-1)]$ decays to $[7_-3, 22(20)]$; deexcitation of one proton from $(dg)_{+1/2}$ to $(dg)_{-1/2}$ and of one neutron from $i_{13/2}$ to $(h_{9/2}f_{7/2})$.

The configurations assigned to the different bands are summarized in Tables II and III. All the three proton configurations are active and they are combined with the neutron configurations which appear most favored according to Fig. 10:

(i) those with all orbitals up to the $N = 78$ gap at $\omega = 0$ filled and in addition two of the three down-sloping orbitals;

(ii) all three down-sloping orbitals filled and then a hole in one of the $\mathcal{N} = 4$ or $\mathcal{N} = 5$ orbitals below the $N = 78$ gap.

The fact that the most favored configurations are active will also mean that the bands which are calculated lowest in energy for $I \approx 30$–35 have an experimental counterpart as illustrated for the $(\pi, \alpha) = (-, 1)$ bands in Fig. 12. Also the $(\pi, \alpha) = (+, 0)$ bands which are calculated to be lowest in energy are assigned to observed bands. For the other parity-signature combinations there are fewer low-lying calculated bands, which is consistent with the fact that fewer such bands are seen according to the tentative (π, I) assignments of the observed high-spin bands.

C. The $\Delta I = 1$ bands interpreted by CSM and TAC calculations

The TAC calculations use the same Hamiltonian as the CNS one. The restriction of CNS that the rotational axis must agree with one of the principal axes is lifted. In order to simplify the calculations, the deformations of the various configurations is kept the same. We use $\varepsilon_2 = 0.17$ and $\gamma = 30^\circ$ as a compromise. Clearly the deviations of the calculations from experiment are expected to be larger than those for the CNS, which optimizes the deformation parameter for each configuration.

In the following we will use the notation that we introduced recently in the paper on the neighboring ^{138}Nd nucleus [11]. The advantage of this notation is the easy translation between single-particle and quasiparticle notation of the orbitals in calculations with or without pairing, which are used to interpret low-medium and high-spin states, respectively. The convention is to use A, B, C, and D for the intruder states h,

TABLE II. Configurations assigned to the high-spin bands of ^{140}Nd. The first column and first line indicate the neutron and proton configurations, respectively, labeled according to Eq. (1). Their total parity and signature is specified in parentheses. The band and its (parity, signature) are indicated at the intersection of each column and line.

	$(d_{5/2}g_{7/2})^8$ $(h_{11/2})^2$ $(+,0)$	$(d_{5/2}g_{7/2})^7_{-1/2}$ $(h_{11/2})^3_{-1/2}$ $(-,1)$	$(d_{5/2}g_{7/2})^7_{1/2}$ $(h_{11/2})^3_{-1/2}$ $(-,0)$
$(s_{1/2}d_{3/2})^{-2}(h_{11/2})^{-2}(h_{9/2}f_{7/2})^2$ $(+,0)$	Q1$(+,0)$	Q7$(-,1)$	
$(s_{1/2}d_{3/2})^{-2}(h_{11/2})^{-2}(h_{9/2}f_{7/2})^1_{-1/2}(i_{13/2})^1_{1/2}$ $(-,0)$	Q5 $(-,0)$	Q12 $(+,1)$	Q8 $(+,0)$
$(s_{1/2}d_{3/2})^{-2}(h_{11/2})^{-2}(h_{9/2}f_{7/2})^1_{1/2}(i_{13/2})^1_{1/2}$ $(-,1)$	Q3 $(-,1)$		
$(s_{1/2}d_{3/2})^{-3}_{1/2}(h_{11/2})^{-2}(h_{9/2}f_{7/2})^2(i_{13/2})^1_{1/2}$ $(+,1)$			Q10 $(-,1)$
$(s_{1/2}d_{3/2})^{-3}_{-1/2}(h_{11/2})^{-2}(h_{9/2}f_{7/2})^2(i_{13/2})^1_{1/2}(+,0)$	Q9 $(+,0)$	Q11 $(-,1)$	

where A is assigned to the lowest state with the favored signature $\alpha = j + 2n$. The letters $E, F, G, H, \ldots$ are used for the normal-parity states (dg), while I is used for $i_{13/2}$. Note also that all occupied orbitals will be specified, which is in line with the CNS labels, but contrary to standard CSM labels [31] where only the occupied "aligned" orbitals are specified.

The bands that we discuss in the present paper have at least two protons and two neutrons excited, which reduces strongly the pair correlations, allowing thus their qualitative interpretation in terms of single-particle configurations in the rotating potential. Figures 14 and 15 show the single-particle Routhians calculated by means of the TAC code [32] for a deformation of $\varepsilon_2 = 0.17$ and $\gamma = 30^\circ$, which is a typical value for this mass region [2,3,6,33,34]. The TAC model considers rotation about an axis that is tilted by the angles θ and ϕ from the principal axes. The long, short, and medium principal axes correspond to (θ, ϕ) equal to (0, 0), (90°, 0), and (90°, 90°), respectively. The different configurations are labeled by the four proton and four neutron orbitals which are occupied outside a "core" with $Z = 56$ and $N = 76$. In the proton core, the six lowest (dg) orbitals outside $Z = 50$ are occupied, while there are four $h_{11/2}$ holes and two (sd) holes below $N = 82$ in the neutron core. From the labels on the orbitals in Figs. 14 and 15, it is then straightforward to see which orbitals are occupied in a specific configuration. Because these labels are defined at a fixed deformation, it becomes possible to specify exactly which orbitals are occupied, contrary to the CNS labels where it is assumed that the lowest orbitals within a specific group are occupied (however, in specific cases, excitations within CNS configurations have been considered; see, e.g., [35,36]).

In this section we apply the unpaired version of the cranked shell model (CSM) [31], which classifies the bands as particle-hole configurations in the rotating potential. The underlying independent particle approximation of the CSM applies only to relative energies and angular momenta.

In contrast to the standard version of CSM we will adopt band Q1 as reference, which is $\pi ABEF \otimes \nu A\bar{A}CD$ in CSM notation or [82,22(20)] in the CNS notation used in the previous section. The composition of the angular momentum is illustrated in Fig. 11. The spins of the two proton particles in $h_{11/2}$ and two neutron particles in $h_{9/2}/f_{7/2}$ are fully aligned, adding to the total angular momentum of $18\hbar$ at the bandhead of Q1.

The experimental Routhian e' and alignment i_x for each band have been extracted following the standard procedure as described, e.g., in Ref. [31], assuming a reference with variable

TABLE III. Experimental and calculated properties of the Q bands in ^{140}Nd. The configuration assignments are given according to Eq. (2).

Band	Experiment			Theory				Excitation type
	α	$E_{\min}$	$I_{\min}$	$\pi = +$		$\pi = -$		
				Configuration	$E_{\min}$	Configuration	$E_{\min}$	
Q1	0	0.5	20	**[82,22(20)]**	0.5			Fragmented decay
Q2	0	0.9	22					Decay to Q1
Q3	1	0.4	27			[82, 22(1_+1)]	0.4	Decay to Q1
Q4	(1)	0.9	(25)					Decay to Q3
Q5	0	0.6	26			[82, 22(1_-1)]	1	Fragmented decay
Q6	0	0.9	26					Decay to Q5
Q7	1	0.5	31			[7$_-$3, 22(20)]	0.5	Decay to Q5 and Q6
Q8	1	0.8	35	[7$_+$3, 22(1_-1)]	0.6			Decay to Q7
Q9	0	0.2	34	[82, 3$_-$2(21)]	−0.2			Decay to Q2 and Q3
Q10	(1)	0.6	(35)			[7$_+$3, 3$_+$2(21)]	0.2	Decay to D10
Q11	(1)	0.2	(41)	[7$_-$3, 3$_-$2(21)]	−0.7			Decay to Q3 and Q10
Q12	(0)	0.3	(32)	[7$_-$3, 22(1_-1)]	0.6			Decay to Q3

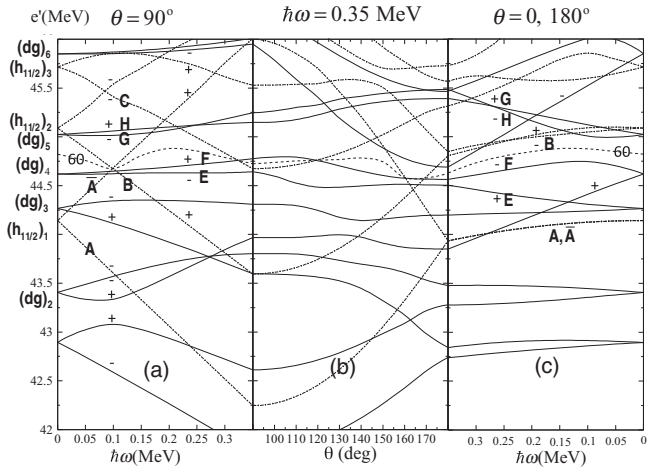

FIG. 14. Calculated single-proton Routhians. Full line $\pi = +$, dash-dotted line $\pi = -$. In case of principal axis rotation the signatures $\alpha = \pm 1/2$ are indicated by $\pm$, respectively. $\theta = 0$ long axis ($\gamma = -90^\circ$), $\theta = 90^\circ$ short axis ($\gamma = 0^\circ$.) The middle panel connects the two axes at the indicated frequency.

moment of inertia $\mathcal{J}^{(0)} + \omega^2 \mathcal{J}^{(2)}$ having the Harris parameters $\mathcal{J}^{(0)} = 7\hbar^2/\text{MeV}$ and $\mathcal{J}^{(2)} = 10\hbar^4/\text{MeV}^3$, which induce a flat behavior of the single-particle alignments of most bands. The projection K of the angular momentum onto the symmetry axis is not a good quantum number in triaxial nuclei. It was put to zero for all bands. From the $e_i{}'(\omega)$ and $i_{i,\text{ref}}(\omega)$ values of a given band i we subtracted the $e_{\text{ref}}{}'(\omega)$ and $i_{\text{ref}}(\omega)$ values of band Q1 calculated at the same frequencies by interpolation with respect to ω. The experimental Routhians e' and the single particle alignments i of the D bands relative to the Q1 reference are shown in the upper panels of Figs. 16 and 17. The reference band Q1 appears as an horizontal line in all figures.

The configurations of the dipole bands in ^{140}N can be understood using TAC calculations similar to those recently performed for the dipole bands in ^{138}Nd [11]. There are one to three $h_{11/2}$ protons and one $h_{9/2}/f_{7/2}$ neutron, which align their angular momentum with the short axis, because this orientation

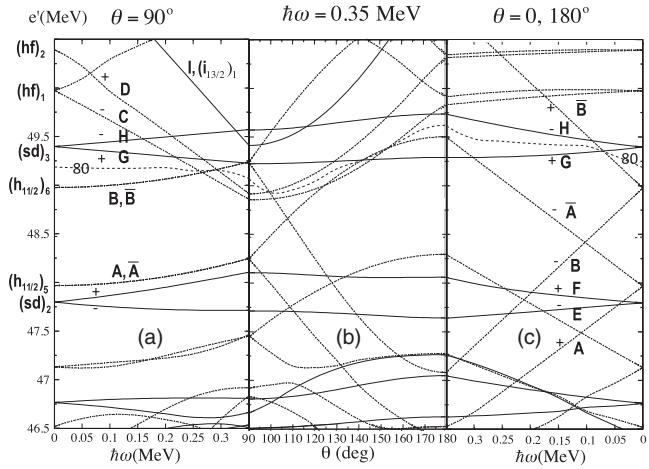

FIG. 15. Calculated single-neutron Routhians. The line and label conventions are similar to those in Fig. 14.

corresponds to maximal overlap of their doughnut-like density distribution with the triaxial core. As a consequence, the $h_{11/2}$ protons and $h_{9/2}/f_{7/2}$ neutrons favor rotation about the short axis. As seen in the middle panels of Fig. 14, the Routhians A and B have a pronounced minimum at $\theta = 90^\circ$. There are also one or two $h_{11/2}$ neutron holes which align their angular momentum with the long axis, because this orientation minimizes the overlap with the triaxial core. As a consequence, the $h_{11/2}$ neutron holes favor rotation about the long axis. As seen in the middle panel of Fig. 15, the Routhians $\bar{A}$ and $\bar{B}$ have pronounced maxima at $\theta = 0^\circ$, which means that holes in these two orbitals drive the rotational axis to $\theta = 0^\circ$. Alternatively one may say that neutrons in A and B orbitals favor the long axis. The $h_{11/2}$ neutrons in the lower orbitals do not drive the rotational axis significantly, because to each Routhian there is a conjugate one (barred) that nearly compensates the drive. The collective angular momentum originating from the rest of the nucleons is maximal for the medium axis, for which the deviation from axial symmetry is maximal.

The experimental Routhians and single-particle assignments of bands D1–D11 relative to the Q1 reference and the corresponding calculated quantities relative to the $\pi h_{11/2}^4 \otimes \nu(h_{9/2}/f_{7/2})^2\,(\pi ABEF \otimes \nu A\bar{A}CD)$ configuration assigned to band Q1 are shown in Figs. 16 and 17.

The large number of dipole bands originates from the combination of $h_{11/2}$ protons and $h_{9/2}/f_{7/2}$ neutrons which align with the short axis, and $h_{11/2}$ neutrons which align with the long axis. The rotational axis lies therefore in the short-long principal plane being tilted away from the principal axes by a large angle. The tilt breaks the $\mathcal{R}_x(\pi)$ symmetry that induces the signature quantum number, and one observes a $\Delta I = 1$ sequence of rotational states, i.e., a dipole band [37]. The rotational mode is predominantly of magnetic nature, because the mutually perpendicular angular momenta of the proton and neutron $h_{11/2}$ orbitals combine to a large transverse magnetic moment, which generates strong $M1$ transitions.

Most of the dipole bands have configurations which contain two $h_{11/2}$ neutron holes that align their angular momentum with the long axis, except the lowest-lying bands D1, D2, and D5 which involve only one $h_{11/2}$ neutron hole. Table IV lists the configurations that originate from these combinations and suggests how to interpret the observed dipole bands. The $B(M1)/B(E2)$ ratios of the dipole bands larger than $20\,\mu_N^2/(e\text{b})^2$ characterize the dipole bands as magnetic rotation.

Band D1 is the lowest excited and has the smallest single-particle alignment. It decays to the 13^- state at 4700 keV whose assigned configuration is $\pi(dg)^4 \otimes \nu h_{11/2}^{-1}(sd)^{-1}\,(\pi A\bar{A}EF \otimes \nu A\bar{A}BG)$ [8]. A configuration that would explain the decay of band D1 towards the 13^- state is $\pi h^2(dg)^2 \otimes \nu h_{11/2}^{-1}(sd)^{-1}$ $(\pi ABEF \otimes \nu A\bar{A}BG)$. Note that the labels specifying the occupation of the j shells refers to a $N = 82$ core while the letter labels $A, B, \ldots$ refer to a $N = 76$ "core."

Band D2 is the next excited dipole band and has a larger single-particle alignment than band D1. It decays to the 15^- state at 5610 keV and to the 17^- state at 6962 keV, with $\pi(dg)^4 \otimes \nu h_{11/2}^{-1}(sd)^{-1}\,(\pi A\bar{A}EF \otimes \nu A\bar{A}BG)$ [8]. We assign the $\pi h^1(dg)^3 \otimes \nu h_{11/2}^{-1}(sd)^{-2}(h_{9/2}f_{7/2})^1\,(\pi A\bar{A}BE \otimes$

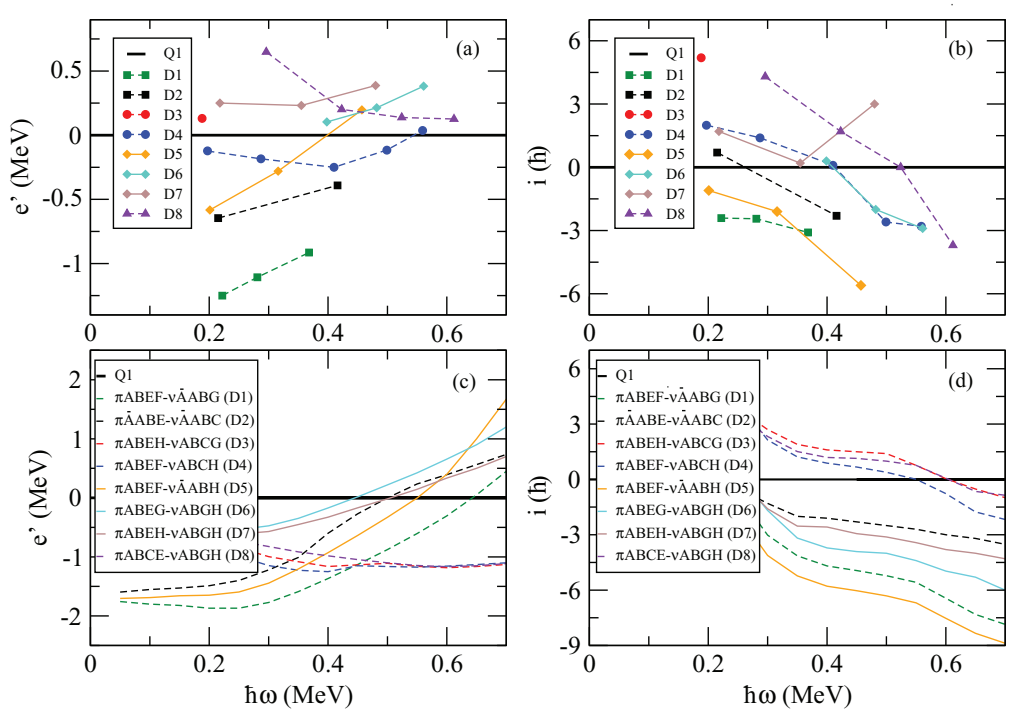

FIG. 16. (Color online) ^{140}Nd $\Delta I = 1$ bands D1–D8. The line type indicates the parity: full $\pi = +$, dashed $\pi = -$.

$\nu A\bar{A}BC$) configuration to band D2, which involves both proton and neutron particle-hole excitations relative to the 15^- and 17^- states towards which it decays.

Band D3 is a short sequence of two transitions, which decays to states of band D4 and to the 20^+ isomer. We assign a $\pi h^2(dg)^2 \otimes \nu h^{-2}_{11/2}(sd)^{-1}(h_{9/2}f_{7/2})^1$ ($\pi ABEH \otimes \nu ABCG$) configuration to this band, which has therefore one additional broken pair relative to the 20^+ isomer, which contribute to the configuration of band D3 with two neutrons in the $h_{11/2}$ and (sd) orbitals, while the two unpaired protons are raised from the (dg) to the $h_{11/2}$ orbital.

Band D4 decays to the 20^+ isomer with a $\pi(dg)^4 \otimes \nu h^{-2}_{11/2}$ ($\pi A\bar{A}EF \otimes \nu ABGH$) configuration and to the 17^- with a state at 6403 keV with a $\pi(dg)^4 \otimes \nu h^{-1}_{11/2}(sd)^{-1}$

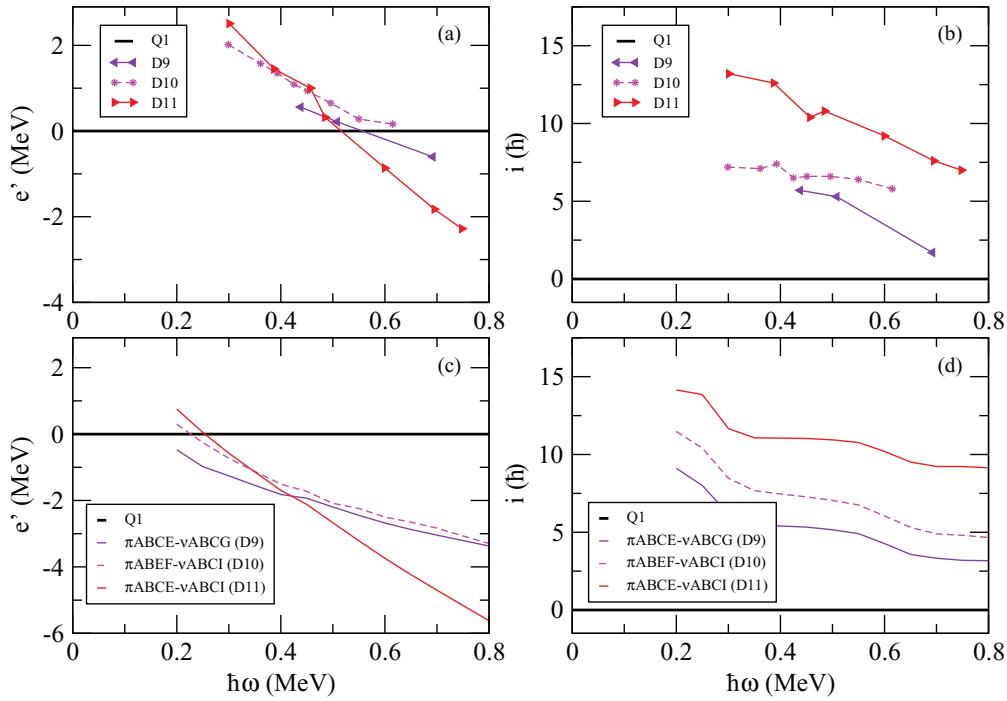

FIG. 17. (Color online) ^{140}Nd $\Delta I = 1$ bands D9–D11. The line type indicates the parity: full $\pi = +$, dashed $\pi = -$.

TABLE IV. Configuration assignments to the $\Delta I = 1$ bands in ^{140}Nd. The calculated $B(M1)/B(E2)$ ratios are in units $\mu_N^2/(e\text{b})^2$.

Configuration	π	$B(M1)/B(E2)$	Bands
$\pi ABEF\ \nu A\bar{A}BG$	$(-)$	93	D1
$\pi A\bar{A}BE\ \nu A\bar{A}BC$	$-$	180	D2
$\pi ABEH\ \nu ABCG$	$-$	213	D3
$\pi ABEF\ \nu ABCH$	$-$	271	D4
$\pi ABEF\ \nu ABGH$	$+$	1331	D5
$\pi ABEG\ \nu ABGH$	$+$	625	D6
$\pi ABEH\ \nu ABGH$	$(+)$	1351	D7
$\pi ABCE\ \nu ABGH$	$(-)$	429	D8
$\pi ABCE\ \nu ABCG$	$(+)$	149	D9
$\pi ABEF\ \nu ABCI$	$(-)$	62	D10
$\pi ABCE\ \nu ABCI$	$(+)$	62	D11

$(\pi A\bar{A}EF \otimes \nu A\bar{A}BG)$ configuration. We assign a $\pi h^2(dg)^2 \otimes \nu h_{11/2}^{-3}(sd)^{-1}(h_{9/2}f_{7/2})^1$ $(\pi ABEF \otimes \nu ABCH)$ configuration to band D4, which is similar to that of band D3. The connecting transitions between bands D3 and D4 are thus explained through a simple one-neutron excitation from the G to the H orbital (see Fig. 15). The connections with the 20^+ isomer and the 17^- state involve more complex excitations, including the scattering of one proton pair from $\pi h_{11/2}^2$ to $\pi(dg)^2$, and a breaking of another neutron pair and the placement of the two aligned neutrons one in $\nu h_{11/2}$ and one in $\nu(h_{9/2}f_{7/2})$.

Band D5 is more excited than bands D1 and D2 and has a very fragmented decay towards states below the 20^+ isomer. It is therefore natural to assign a configuration with one more neutron in $h_{11/2}$ relative to the configurations of bands D1 and D2. The parity of band D5 is positive, being well established by the 1366 keV $E2$ transition towards the 16^+ state. The configuration that we assign to band D5 is the lowest-lying positive-parity configuration involving 2 $h_{11/2}$ neutrons and 2 $h_{11/2}$ protons, that is $\pi h^2(dg)^2 \otimes \nu h_{11/2}^{-2}$ $(\pi ABEF \otimes \nu ABGH)$.

Band D6 decays to band D5 and has a larger alignment. In order to account for the higher excitation energy of band D6 relative to D5, we can excite one proton from the F to the G positive-parity orbital, leading to the $\pi h^2(dg)^2 \otimes \nu h_{11/2}^{-2}$ $(\pi ABEG \otimes \nu ABGH)$ configuration. However, the calculated difference in spin alignment between the bands D5 and D6 does not agree with the experimental value. This effect can be induced by the difference between the deformation used in the calculations and the real deformation of the configurations of bands D5 and D6.

Band D7 has an excitation very similar to band D6 and possibly a positive parity. We can then assign a configuration similar to that of band D6, with one proton moved from the G to the H orbital, that is the $\pi h^2(dg)^2 \otimes \nu h_{11/2}^{-2}$ $(\pi ABEH \otimes \nu ABGH)$ configuration.

Band D8 is more excited and has a larger alignment than the bands D6 and D7 to which it decays. A configuration which would account for that is obtained by rising one more proton in $h_{11/2}$. We assign the $\pi h^3(dg)^1 \otimes \nu h_{11/2}^{-2}$ $(\pi ABCE \otimes \nu ABGH)$ configuration to band D8.

Band D9 starts at spin 28^-, which can be obtained involving eight active nucleons, one of which being a neutron in the $(h_{9/2}f_{7/2})$ orbital, which would account for its decay to band Q1 with $\pi h^2(dg)^2 \otimes \nu(h_{9/2}f_{7/2})^2$ configuration. In order to realize the condition for a tilted axis rotation the presence of nearly equal numbers of particles aligned along the short and long axes is necessary. A possible configuration can then be $\pi h^3(dg)^1 \otimes \nu h_{11/2}^{-2}(sd)^{-1}(h_{9/2}f_{7/2})^1$ $(\pi ABCE \otimes \nu ABCG)$.

Band D10 has both dipole and quadrupole crossover transitions, indicating lower $B(M1)/B(E2)$ branching ratios than the rest of the dipole bands excepting D11. As it starts at spin 25^- which is lower than the band-head spin of D9 which is assigned an eight-particle configuration, it can also have a configuration with eight active particles, that is $\pi h^2(dg)^2 \otimes \nu h_{11/2}^{-2}(sd)^{-2}(h_{9/2}f_{7/2})^1 i_{13/2}^1$ $(\pi ABEF \otimes \nu ABCI)$.

Band D11 has both dipole and quadrupole crossover transitions, indicating lower $B(M1)/B(E2)$ branching ratios. It is the highest excited dipole band observed in the experiment, and can have a configuration with eight active particles like band D10, but with one more proton raised in the $h_{11/2}$ orbital, that is $\pi h^3(dg)^1 \otimes \nu h_{11/2}^{-2}(sd)^{-2}(h_{9/2}f_{7/2})^1 i_{13/2}^1$ $(\pi ABCE \otimes \nu ABCI)$.

V. SUMMARY

High-spin states in ^{140}Nd have been populated using the reaction ^{96}Zr(^{48}Ca,4n) and two powerful setups: EUROBALL and JUROGAM II + RITU + GREAT. The prompt γ-γ coincidences measured with EUROBALL and JUROGAM II and the prompt-delayed coincidences between the γ rays measured at the target position and at the focal plane of the RITU spectrometer allowed the identification of many new transitions, among which are also those populating the 20^+ isomer. A very rich and complete level scheme was developed and most of the existing information was confirmed. New bands of quadruple and dipole transitions were identified up to very high spin. The observed bands were discussed using the TAC and CNS models. Possible configurations for the different bands are discussed, showing that rotations can occur in ^{140}Nd either around a principal or a tilted axis of the intrinsic reference system, depending on the presence in the configurations of protons and neutrons in the $h_{11/2}$ orbitals. The global understanding of the observed bands brings a strong support to the existence of a stable triaxial deformation at high spin in this mass region.

ACKNOWLEDGMENTS

This work was supported by Swedish Natural Science Research Council. C.P. acknowledges the Japan Society for the Promotion of Science (JSPS) under the "FY2011 JSPS Invitation Fellowship Program for Research in Japan." S.F. acknowledges DOE Grant No. DE-FG02-95ER4093. For the JUROGAM II experiment we acknowledge the EU-FP7 Integrating Activities Project ENSAR (No. 262010), the Academy of Finland under the Finnish Centre of Excellence Programme 2006-2011 (Contract No. 131665), and the European GAMMAPOOL network (EUROBALL owners committee) for providing the detectors of JUROGAM II. The

authors thank the GABRIELA Collaboration for the loan of the TNT2D cards. The work of the Bonn group was supported by BMBF, Germany, under Contracts No. 06 BN 07 and No. 06 BN 109. The EUROBALL was supported by the EU under Contract No. HPRI-CT-1999-00078, by the Italian National Institute of Nuclear Physics (INFN), by the Danish Science Foundation, by the Swedish Science Research Council, and by the DOE under Contract No. DE-AC03-76SF00098.

[1] P. Möller, J. R. Nix, W. D. Myers, and W. J. Swiatecki, At. Data Nucl. Data Tables **59**, 185 (1995).
[2] C. M. Petrache, G. Lo Bianco, D. Ward, A. Galindo-Uribarri, P. Spolaore, D. Bazzacco, T. Kröll, S. Lunardi, R. Menegazzo, C. Rossi Alvarez, A. O. Macchiavelli, M. Cromaz, P. Fallon, G. J. Lane, W. Gast, R. M. Lieder, G. Falconi, A. V. Afanasjev, and I. Ragnarsson, Phys. Rev. C **61**, 011305(R) (1999).
[3] C. M. Petrache, M. Fantuzi, G. Lo Bianco, D. Mengoni, A. Neusser-Neffgen, H. Hübel, A. Al-Khatib, P. Bringel, A. Bürger, N. Nenoff, G. Schönwasser, A. K. Singh, I. Ragnarsson, G. B. Hagemann, B. Herskind, D. R. Jensen, G. Sletten, P. Fallon, A. Görgen, P. Bednarczyk, D. Curien, G. Gangopadhyay, A. Korichi, A. Lopez-Martens, B. V. T. Rao, T. S. Reddy, and N. Singh, Phys. Rev. C **72**, 064318 (2005).
[4] A. Neußer, H. Hübel, A. Al-Khatib, P. Bringel, A. Bürger, N. Nenoff, G. Schönwasser, A. K. Singh, C. M. Petrache, G. Lo Bianco, I. Ragnarsson, G. B. Hagemann, B. Herskind, D. R. Jensen, G. Sletten, P. Fallon, A. Görgen, P. Bednarczyk, D. Curien, G. Gangopadhyay, A. Korichi, A. Lopez-Martens, B. V. T. Rao, T. S. Reddy, and N. Singh, Phys. Rev. C **70**, 064315 (2004).
[5] N. Yoshikawa, Nucl. Phys. A **243**, 143 (1974).
[6] S. Bhowal, G. Gangopadhyay, C. M. Petrache, I. Ragnarsson, A. K. Singh, S. Bhattacharya, H. Hübel, A. Neußer-Neffgen, A. Al-Khatib, P. Bringel, A. Bürger, N. Nenoff, G. Schönwasser, G. B. Hagemann, B. Herskind, D. R. Jensen, G. Sletten, P. Fallon, A. Görgen, P. Bednarczyk, D. Curien, A. Korichi, A. Lopez-Martens, B. V. T. Rao, T. S. Reddy, and N. Singh, Phys. Rev. C **84**, 024313 (2011).
[7] E. Gulmez, H. Li, and J. A. Cizewski, Phys. Rev. C **36**, 2371 (1987).
[8] C. M. Petrache, R. A. Bark, S. T. H. Murray, M. Fantuzi, E. A. Lawrie, S. Lang, J. J. Lawrie, S. M. Maliage, D. Mengoni, S. M. Mullins, S. S. Ntshangase, D. Petrache, T. M. Ramashidzha, and I. Ragnarsson, Phys. Rev. C **74**, 034304 (2006).
[9] M. Ferraton, R. Bourgain, C. M. Petrache, D. Verney, F. Ibrahim, N. de Séréville, S. Franchoo, M. Lebois, C. Phan Viet, L. Sagui, I. Stefan, J. F. Clavelin, and M. Vilmay, Eur. Phys. J. A **35**, 167 (2008).
[10] A. Vancraeyenest, C. M. Petrache, D. Guinet, P. T. Greenlees, U. Jakobsson, R. Julin, S. Juutinen, S. Ketelhut, M. Leino, M. Nyman, P. Peura, P. Rahkila, P. Ruotsalainen, J. Saren, C. Scholey, J. Sorri, J. Uusitalo, P. Jones, C. Ducoin, P. Lautesse, C. Mancuso, N. Redon, O. Stezowski, P. Desesquelles, R. Leguillon, A. Korichi, T. Zerrouki, D. Curien, and A. Takashima, Phys. Rev. C **87**, 064303 (2013).
[11] C. M. Petrache, S. Frauendorf, M. Matsuzaki, R. Leguillon, T. Zerrouki, S. Lunardi, D. Bazzacco, C. A. Ur, E. Farnea, C. Rossi Alvarez, R. Venturelli, and G. de Angelis, Phys. Rev. C **86**, 044321 (2012).
[12] P. J. Nolan, F. A. Beck, and D. B. Fossan, Annu. Rev. Nucl. Part. Sci. **45**, 561 (1994).
[13] M. Leino, J. Äistö, T. Endqvist, P. Heikkinen, A. Jokinen, M. Nurmia *et al*., Nucl. Instrum. Methods B **99**, 653 (1995).
[14] R. D. Page *et al*., Nucl. Instrum. Methods B **204**, 634 (2003).
[15] I. Lazarus *et al*., IEEE Trans. Nucl. Sci. **48**, 567 (2001).
[16] P. Rahkila, Nucl. Instrum. Methods A **595**, 637 (2008).
[17] O. Stezowski, http://agata.in2p3.fr/gw/doxy.
[18] D. C. Radford, Nucl. Instrum. Methods A **361**, 297 (1995).
[19] D. C. Radford, Nucl. Instrum. Methods A **361**, 306 (1995).
[20] J. Simpson, Z. Phys. A **358**, 139 (1997); F. A. Beck, Prog. Part. Nucl. Phys. **28**, 443 (1992).
[21] T. Bengtsson and I. Ragnarsson, Nucl. Phys. A **436**, 14 (1985).
[22] A. V. Afanasjev, D. B. Fossan, G. J. Lane, and I. Ragnarsson, Phys. Rep. **322**, 1 (1999).
[23] B. G. Carlsson and I. Ragnarsson, Phys. Rev. C **74**, 011302(R) (2006).
[24] K. Pomorski and J. Dudek, Phys. Rev. C **67**, 044316(R) (2003).
[25] T. Bengtsson, Nucl. Phys. A **512**, 124 (1990).
[26] M. Mustafa *et al*., Phys. Rev. C **84**, 054320 (2011).
[27] B. G. Carlsson and I. Ragnarsson, Phys. Rev. C **70**, 024303 (2004).
[28] J. Gellanki *et al*., Phys. Rev. C **86**, 034304 (2012).
[29] A. Galindo-Uribarri, D. Ward, G. C. Ball, V. P. Janzen, D. C. Radford, I. Ragnarsson, and D. Headly, Phys. Lett. B **422**, 45 (1998).
[30] C. E. Svensson, C. Baktash, G. C. Ball, J. A. Cameron, M. Devlin, J. Eberth, S. Flibotte, A. Galindo-Uribarri, D. S. Haslip, V. P. Janzen, D. R. LaFosse, I. Y. Lee, A. O. Macchiavelli, R. W. MacLeod, J. M. Nieminen, S. D. Paul, D. C. Radford, L. L. Riedinger, D. Rudolph, D. G. Sarantites, H. G. Thomas, J. C. Waddington, D. Ward, W. Weintraub, J. N. Wilson, A. V. Afanasjev, and I. Ragnarsson, Phys. Rev. Lett. **80**, 2558 (1998).
[31] R. Bengtsson and S. Frauendorf, Nucl. Phys. A **327**, 139 (1979).
[32] S. Frauendorf, Nucl. Phys. A **557**, 250c (1993); **677**, 115 (2000).
[33] C. M. Petrache, D. Bazzacco, S. Lunardi, C. Rossi Alvarez, R. Venturelli, D. Bucurescu, C. A. Ur, D. De Acuna, G. Maron, D. R. Napoli, N. H. Medina, J. R. B. Oliveira, and R. Wyss, Phys. Lett. B **373**, 275 (1996).
[34] C. M. Petrache, R. Venturelli, D. Vretenar, D. Bazzacco, G. Bonsignori, S. Brant, S. Lunardi, M. A. Rizzutto, C. Rossi Alvarez, G. de Angelis, M. De Poli, and D. R. Napoli, Nucl. Phys. A **617**, 228 (1997).
[35] D. Karlgren *et al*., Phys. Rev. C **69**, 034330 (2004).
[36] D. Rudolph *et al*., Phys. Rev. Lett. **96**, 092501 (2006).
[37] S. Frauendorf, Rev. Mod. Phys. **73**, 463 (2001).